Experimental and numerical investigation of I-beam to concrete-filled tube (CFT) column moment connections with pipe-stiffened internal diaphragm

Alireza Habibi [a], Nader Fanaie [b], Shahriar Shahbazpanahi [a],*

[a] *Department of Civil Engineering, Sanandaj Branch, Islamic Azad University, Sanandaj, Iran*
[b] *Department of Civil Engineering, K. N. Toosi University of Technology, Tehran, Iran*

ARTICLE INFO

ABSTRACT

This paper presents an experimental and numerical investigation of two full-scale I-beam to concrete-filled tube (CFT) column internal-diaphragm moment connection specimens. In this type of connection, to allow the passage of concrete through the column tube wall, the internal diaphragms are perforated, which, as a result of drilling, creates stress concentration in these plates, reducing their strength and stiffness. In this study, first, to improve the diaphragms' performance, these plates were stiffened utilizing steel pipes, and the effect of this stiffening on the connection behavior under cyclic loading was investigated in the laboratory. In the second part, the specimens were analyzed by the finite element (FE) method in the Abaqus software. Results indicated that stiffening the internal diaphragm plates with the pipes increased the connection's flexural strength and cumulative energy dissipation by 20% and 22%, respectively. It also prevented the yielding of the diaphragm plates and increased the connection's stiffness by 8% to 22%. Furthermore, the stiffening of the internal diaphragms led to better stress distribution at the plastic hinge region in the beam and shifting of the maximum rupture index location from the outer edge of the beam flanges by about 40% of the beam flange width towards the beam's longitudinal axis. It was also concluded that the proposed connection with stiffened internal diaphragm meets the criteria for utilization in intermediate moment frames (IMFs) in seismic regions.

1. Introduction

Concrete-filled tube (CFT) columns, constructed using both concrete and steel, simultaneously provide the advantages of each of the two mentioned common building materials. Through the joint contribution of concrete and steel, a structural member with excellent properties such as high load-bearing capacity in compression, bending, shear and torsion is created. CFT columns have high energy absorption capacity and suitable ductility and are appropriate for use in seismic regions. The steel boxes in these columns eliminate the need for molding, enabling a quick fabrication process. CFT columns are also more economical than concrete and steel columns [1–3]. Also, the steel tube creates the confinement effect for the concrete core and, as a result, increases its compressive strength and ductility [4]. Since the 1970s, research has shown that moment frames with CFT columns and I-beams are much more efficient than conventional steel or reinforced concrete structures, and hence, they have been widely used in mid-height and tall buildings in Japan [5]. One of the advantages of CFT columns is their high stiffness; therefore, they could be used to control the displacements of

buildings with moment frames by increasing their stiffness. However, the necessity of pouring concrete inside the CFT columns makes it very difficult to assemble the continuity plates at the connection zone [6].

Various methods have been proposed to eliminate continuity plates, but most are still under investigation and have not been yet included in the building codes. Jahanbakhti et al. investigated the possibility of eliminating the continuity plates in I-beam to column moment connections by theoretical and experimental approaches. Assuming the elimination of the continuity plates and using theoretical methods, they determined the column web and flange thicknesses in the connection zone and subjected the full-scale laboratory specimens to cyclic loading [7]. Hosseini and Rahnavard proposed innovative short and large collar connections to eliminate the continuity plates in box-columns by the FE method. It was found that the seismic behavior of the large collar connection is favorable, and it can be utilized in special steel moment frame systems [8].

In moment connections, the continuity plates are utilized inside the column to distribute the forces evenly and prevent local instabilities of the column components, and their poor performance can lead to weak connection behavior. According to AISC 360–16 and AISC-341-16,

---

Nomenclature

b	inside width of the column tube
b_f	width of beam flange
CFT	concrete-filled tube
CPJ	complete joint penetration
d_b	overall depth of beam
E	young's modulus of the steel
ESW	electro slag welding
FE	finite element
F_y	yield stress of the steel
F_u	tensile strength of the steel
h_w	height of beam web
IMF	intermediate moment frame
K_i	secant stiffness in the story drift angle i
K_0	initial stiffness
LVDT	linear variable displacement transducer
M_{pb}	nominal plastic moment strength of the beam
M_{pc}	nominal plastic moment strength of the column
$(M_{pr})_b$	maximum probable moment at the location of the plastic hinge of the beam
M_i^j	maximum bending moment in the jth cycle of the story drift angle i
PEEQ	plastic equivalent strain index

SCC	self-compacting concrete
SMF	special moment frame
t	flange and web thickness of column
t_f	thickness of beam flange
t_w	thickness of beam web
WUF-W	welded unreinforced flange-welded web
Z_b	plastic section modulus of the beam
β	stiffness degradation coefficient
ε_p	equivalent plastic strain
ε_y	yield strain
θ_i^j	story drift angle corresponding to M_i^j
μ	friction coefficient between steel tube and concrete core
ν	poisson's ratio of the steel
σ_{eff}	von mises stress
σ_m	hydrostatic stress
$\sum M_{pc}^*$	sum of the projections of the nominal flexural strengths of the columns above and below the joint to the beam centerline
$\sum M_{pb}^*$	sum of the projections of the expected flexural strengths of the beams at the plastic hinge locations to the column centerline
f'_c	specified compressive strength of the concrete
$\frac{\sigma_m}{\sigma_{eff}}$	triaxiality ratio (TR)

moment connections must have sufficient rigidity and ductility and transfer the bending moment of the beam to the column. To provide ductility in the joint, the minimum rotation capacity due to inter-story drift angle in the inelastic range is required to be 0.03 rad in special moment frames (SMFs) and 0.01 rad in intermediate moment frames (IMFs) [9,10].

Beam to CFT column moment connections are fabricated in different ways, each with advantages and disadvantages. Because of the tension and compression created in the beam flanges caused by the connection moment, a large shear force is created in the panel zone borne by the column tube wall and diagonal concrete compression [11]. In CFT columns, due to the presence of concrete filling the steel tube, it is not possible to use continuity plate similar to those incorporated in steel box columns, and it is necessary to strengthen these columns at the beam to column connections using other methods, the most common of which are as shown in Fig. 1 [12].
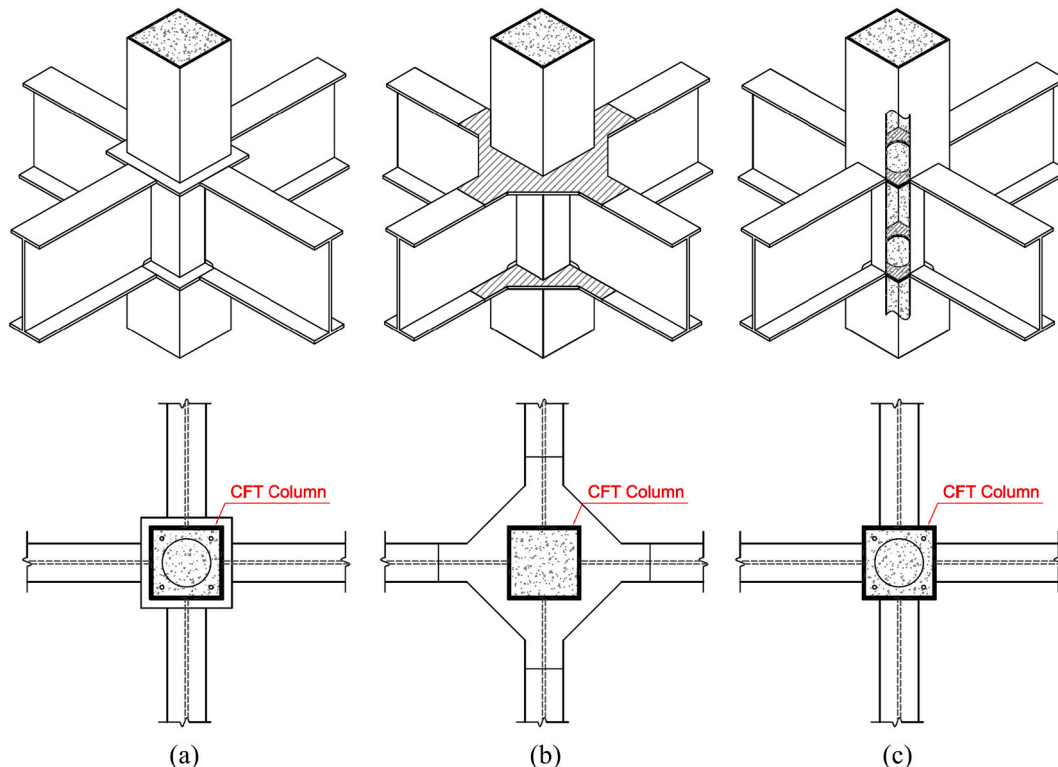

Fig. 1. Connections with: a) Through diaphragms; b) External diaphragms; c) Internal diaphragms [12].

Internal and through diaphragms have openings that allow concrete passage and sometimes also feature vent holes for better concrete curing, which according to the Chinese specification are recommended to be at least 25 mm in diameter [13,14]. Internal diaphragms are usually used for high-rise buildings with box columns, and their openings should be large enough so that the tremie pipe can pass through them, and the concrete fills inside the column and panel zone. These diaphragms are very practical and economical for columns with very large dimensions, where the welder can go inside the column and perform the welding of the continuity plates to the column. For smaller columns, diaphragms are first welded to three sides of the column, and the welding to the fourth side of the column is done by dividing it into three sections or using electro slag welding (ESW) [15].

Yaghoobi Zadeh and Fanaie, through analysis of moment connections with internal diaphragms by FE method, showed that internal diaphragms with circular openings are a better option than other forms of drilling because of better stress distribution [16]. Doung et al. investigated beam to box-column moment connections with and without concrete filling using experimental and theoretical methods and provided the relationships for designing internal diaphragms [17].

Qin et al. suggested a new type of internal-diaphragm I-beam to CFT column moment connections strengthened using tapered plates along the beam flanges at the beam-column interface. They reported that the proposed connection type could be used in intermediate moment frames in seismic regions [18].

Internal diaphragms do not interfere with the beam to column connection mechanism. Nonetheless, due to the significant moment transferred to diaphragms from the connection, the stress concentration around the openings in these plates increases, and hence they must be strengthened with a suitable approach. Increasing the thickness of the diaphragm plates or reducing the diameter of the openings can improve stress distribution. However, increasing the thickness of these plates also increases welding volume, residual stresses and the possibility of column tube wall deformation. Reducing the openings' diameter also hinders concrete passage and increases the likelihood of the concrete honeycombing at the connection zone. Xiao and Zhang presented the FE analysis of moment connections using internal-diaphragm. They concluded that the seismic behavior of the connections with internal diaphragms with three welded edges, which are easier to construct, is not much different from those with internal diaphragms with four welded edges [19]. Doung and Sasaki, through a theoretical and numerical study of the beam to column moment connections with internal diaphragms with circular openings, concluded that larger diaphragm or column dimensions lead to better connection performance. Also, they found that the thickness, diameter and shape of the diaphragm openings play the most important role in changing the connection strength [20]. In other studies, Nie et al. compared the seismic behavior of composite beam to CFT column moment connections with internal diaphragms and those with the shear studs welded to the column wall at the panel zone. They found that connections with internal diaphragms have good strength but low ductility [21,22].

There are no obstacles blocking the concrete passage at the panel zone in connections with external diaphragms. However, these stiffeners at the beam to column connection interfere with the structure's architectural design and the connection of the beams. The methods for calculating the panel zone strength in connections using external diaphragm are provided in structural design provisions by the Architectural Institute of Japan [23]. These connections shift the plastic hinge away from the column wall, making it less likely to rupture at the beam to column connection [24].

In fabricating through diaphragm connections, the column is divided into three sections of upper, lower and connection zone, and each section is connected to the diaphragm plates through fillet or CPJ groove welds. Nonetheless, such connections have not become very popular due to the necessity of cutting the column and extensive welding at the connection zone. Rong et al. investigated the hysteresis behavior of

three frames with moment connections and through diaphragms under cyclic loading by experimental and numerical methods. In order to investigate weak panel zones, they reduced the tube wall thickness of the CFT columns at the panel zones in two of the specimens. The fracture modes observed included the buckling of the column webs and flanges at the panel zone and weld ruptures in the connection region [25].

Lu et al. tested beam to CFT column moment connections with internal, external and through diaphragms. They found that external diaphragms have the highest shear strength and the lowest ductility, and internal diaphragms have the highest ductility and the lowest shear strength. Through diaphragms exhibited similar shear strength to internal diaphragms but lower ductility [26]. Filling box columns with concrete increase the initial stiffness and maximum load-bearing capacity of beam-to-column moment connections with horizontal and vertical diaphragms. The shape of the edges of diaphragm openings and their reinforcement also affects the initial stiffness and connection strength [27]. Choi et al. tested four beam to CFT column moment connection specimens with perforated internal diaphragms, perforated through diaphragms, combined perforated diaphragms and pipe-reinforced combined diaphragms. All of the specimens failed at the drift angle of 0.03 rad [28].

In some cases, architectural limitations or seismic provisions in building codes force us to utilize moment frames, in which beam-to-column connections must be rigid. In these connections, external diaphragms or continuity plates (internal diaphragms or through diaphragms) must be utilized to properly transfer the large amounts of forces due to bending moment from the beam flanges to the column. In CFT columns, to allow the passage of concrete through the column tube wall, the continuity plates need to be perforated, which reduces their strength and stiffness and hence decreases the connection's flexural performance. In this study, steel pipes were utilized to stiffen the internal diaphragms, and by conducting a detailed full-scale experimental study, the effect of this reinforcement on the seismic behavior of the rigid beam to the CFT column connection was investigated. Stiffening the internal diaphragms with pipe may increase the stiffness and strength of these plates and improve the seismic behavior of the connection.

Experimental results, including hysteresis curves, cumulative dissipated energy, stiffness degradation, connection failure modes and strain values in the plastic hinges formed, were compared for a specimen with the pipe-stiffened continuity plate and a similar specimen with a non-stiffened continuity plate. It should be noted that in all previous researches, no effective solution has been presented to stiffen the perforated continuity plate with the pipe.

2. Experimental investigation

2.1. Specimens

Specimens in this study included two I-beam to CFT column connections, built according to the AISC 358–10 specifications for the prequalified welded unreinforced flange-welded web (WUF-W) moment connection. According to the provisions of this standard, in these specimens, the beam web and flanges and the single shear tab were connected to the column flange using CJP groove welds [29]. The specimens were constructed as T-shaped exterior joints connecting a beam to a column with sections similar to those in a 15-story special moment frame steel building. The support conditions selected were such that the beam and column deflections in the specimens resembled those of members in moment frames subjected to lateral loads. Accordingly, the two column ends and the beam end in the specimens were considered as the inflection points in the middle of such members in a moment frame undergoing lateral loads in the form of hinge supports (Fig. 2). Figs. 3 & 4 shows the configuration of the tests performed. It can be seen that the actuator applies horizontal movement along the column axis to the tip of the beam. Furthermore, Fig. 5 illustrates the location of the strain gauges
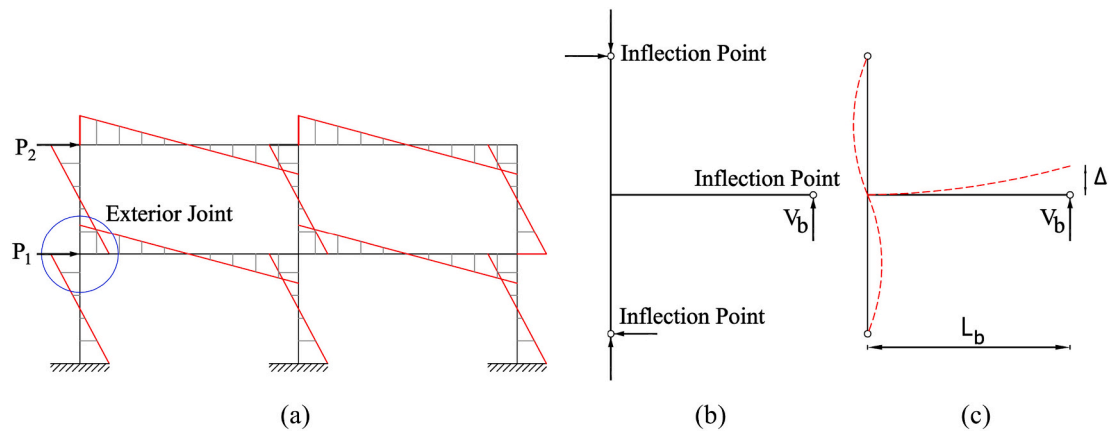
Fig. 2. Exterior joint in a moment frame: a) Frame subjected to lateral load; b) Idealized exterior joint; C) Angular rotation.
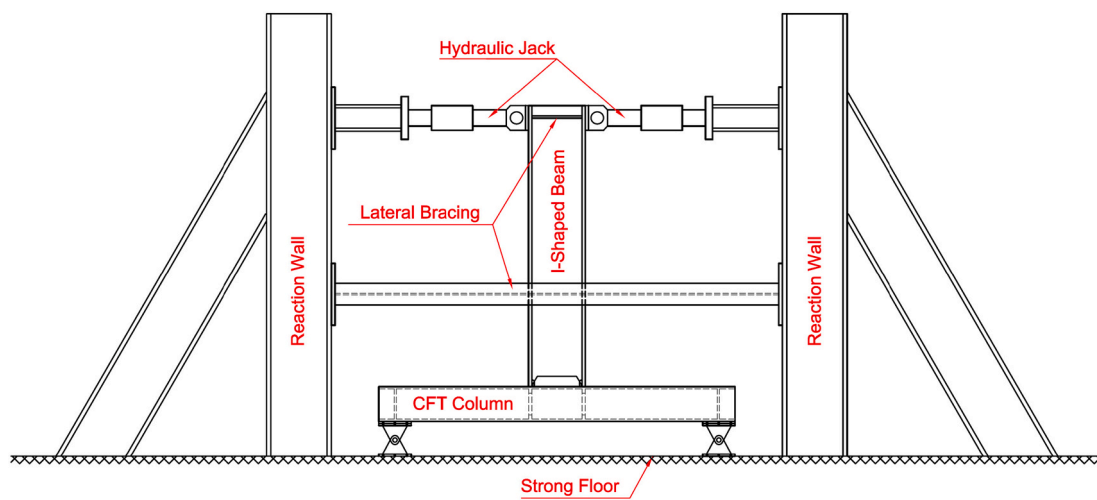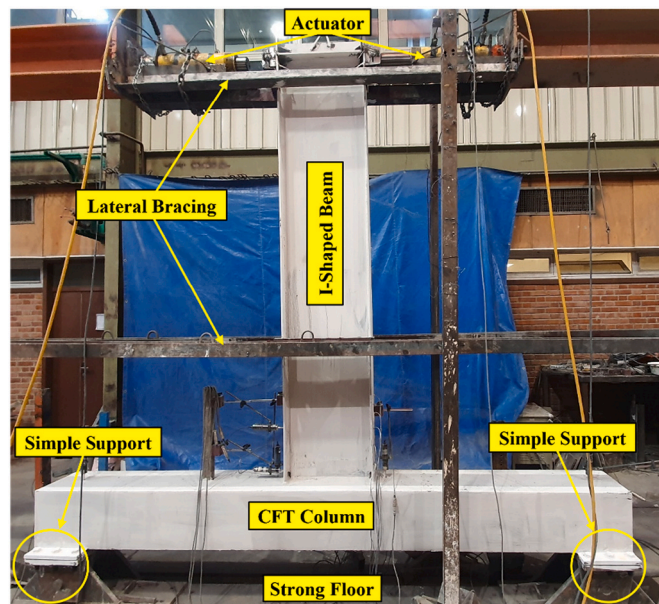

Fig. 3. Test setup arrangement.

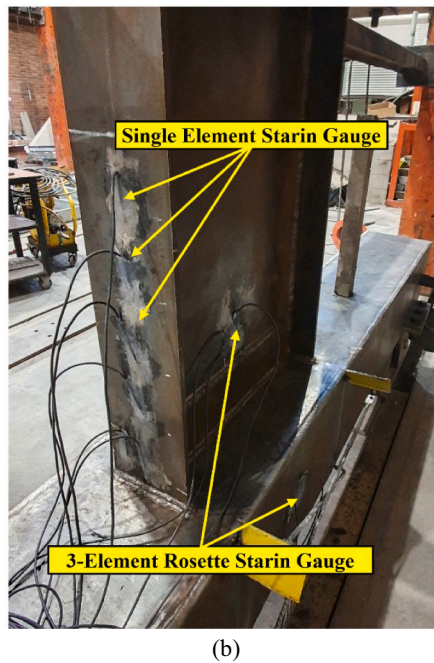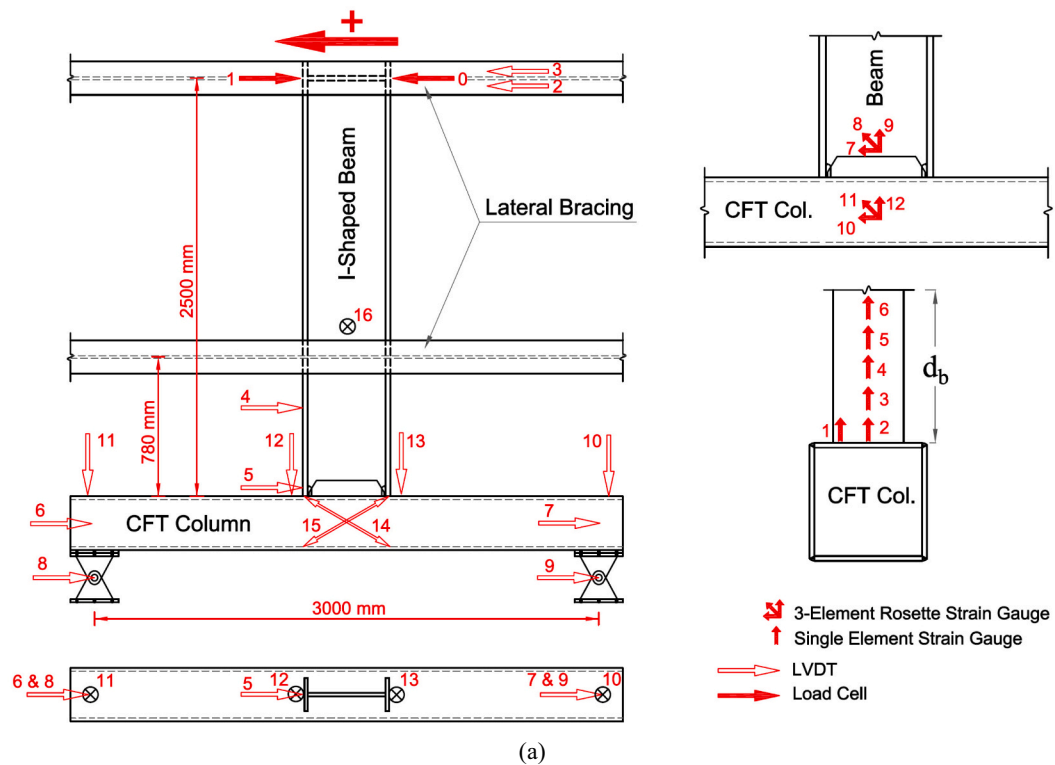**Fig. 4.** Configuration of the tests performed.

(a)

(b)

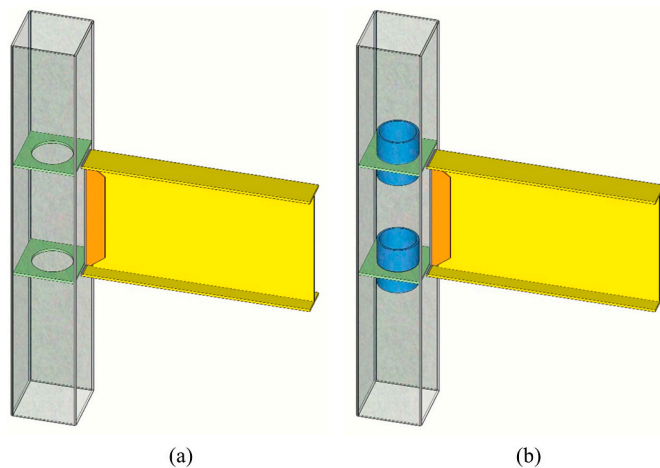**Fig. 5.** Strain gauges and LVDTs installation locations.

Fig. 6. Tested connection specimens: a) Specimen 1: Internal diaphragm (ID); b) Specimen 2: Stiffened internal diaphragm with pipe (SID).

and LVDTs used to measure the displacements during loading. The hydraulic jack in the configuration applied the intended cyclic displacement according to the loading protocol specified by AISC 341–16. In order to prevent lateral-torsional buckling of the beam, lateral bracings were utilized per the AISC provisions.

The width to thickness ratios of the beam and column components were determined according to the AISC 341–16 seismic provisions to prevent the local buckling in the members before the formation of the plastic hinge in the beam, which leads to decreasing the load-bearing capacity [11]. Creating openings in the diaphragm plates for concrete passage weakens these plates and cuts off the transfer path of the connection's force due to bending moment. In this study, it has been attempted to solve this issue by stiffening the diaphragm plates with pipes to improve their performance and thus improve the overall performance of the connection. Fig. 6 illustrates the tested connection specimens using internal-diaphragm and stiffened internal-diaphragm, referred to as specimen 1 (ID) and specimen 2 (SID), respectively.

2.2. Specimens' details

The I-beam and box-column sections in the two full-scale laboratory specimens, shown in Fig. 6, were built using steel plates and pipe, which were subjected to standard tensile and Charpy tests. The properties and mechanical specifications of plates, pipe and design parameters of the specimens are given in Tables 1 to 4.

The connection design was done according to the seismic provisions of AISC 341–16 for special moment frames. The strong column-weak beam criteria, panel zone shear, the maximum beam shear under the

effect of the hydraulic jack during loading and the lateral beam bracing intervals were also controlled and determined accordingly [10]. The internal diaphragms in the specimens were designed with circular openings to reduce stress concentration within them. The Eurocode 4 guidelines for the dimensions and specifications of openings in internal diaphragms, shown in Fig. 7, were also followed accordingly [30]. In the constructed specimens, the diameter of the internal diaphragm openings was large enough for the tremie pipe to pass easily through them, and thus concrete pouring could be done without considerable free-fall leading to concrete segregation.

Furthermore, because the height of the columns was about 3 m, it was not possible to use a needle vibrator for suitable concrete compaction. Therefore, self-compacting concrete (SCC), which does not require vibration, was used to fill the columns in the specimens. The mixture proportions of the SCC poured inside the column tubes are given in Table 5. Round river aggregate with an absorption capacity of 0.5% was selected for use as coarse aggregate. River sand with a fineness modulus of 2.9 and an absorption capacity of 1.62% was also selected as a natural fine aggregate.

Figs. 8 and 9 present the detailed drawings of the specimens. The CJP groove welds were all made using the E7018 electrode. The charpy impact toughness of this electrode is sufficient for the rigid connection of the beam to the column in special moment frames, and the weld does not experience cracks and ruptures during cyclic loading, also allowing a more detailed analysis of the diaphragm plates' behavior. The E7018 electrode is also compatible with base metal and has a higher strength than base metal [10].

For building-up a box column reinforced with internal diaphragms, a U-shaped section is built first. Then, all three sides of the diaphragms were welded using CJP groove welds. The prepared U-shaped section is covered and welded by a plate with limit length as the box column's fourth side. The diaphragm is manually welded to the fourth side of the box column by a welder. The fourth sides of the box column are welded to the U-shaped section at each story level, and the remaining parts are completed and welded. Fig. 10 shows the columns in the specimens before the welding of the plates on their fourth side. As shown in the detailed drawings presented in Figs. 8 and 9, the beams were connected to the side of the columns opposite to their fourth side.

Table 2
Mechanical specifications of the pipes used to stiffen the internal diaphragms.

Length (mm)	Outside Diameter(mm)	Thickness (mm)	F_y (MPa)	F_u (MPa)	Elongation (%)
200	219.1	10	271.6	495.3	28.9

Table 1
Mechanical specifications of the plates and concrete utilized to construct specimens.

Steel							Concrete
Member	Thickness (mm)	F_y (MPa)	F_u (MPa)	Elongation (%)	Toughness(J) 20(°C)	Toughness(J) −20(°C)	f '$_c$(MPa)
Beam web	8	307.6	481.8	35	–	–	50
Beam Flange	10	304.8	425.6	29	289.7	213.6	
Column & Internal Diaphragm	10	289.2	412.6	32	288.1	68.7	

Table 3
Design parameters of the columns and internal diaphragms.

Spec. No.	Name	Column Tube (mm x mm x mm)	$\left(\frac{b}{t}\right)_c$	Internal Diaphragm Thickness(mm)	Internal Diaphragm Hole(mm)	Concrete infill	Stiffened Internal Diaphragm with Pipe	M_{pc}(kN.m)
1	ID	$320 \times 320 \times 10$	30	10	199.1	SCC	No	386.48
2	SID	$320 \times 320 \times 10$	30	10	199.1	SCC	Yes	386.48

Table 4
Design parameters of the beams.

Name	Built-up I-beam d_b (mm)	b_f (mm)	t_f (mm)	t_w (mm)	$\left(\frac{b_f}{2t_f}\right)_b$	$\left(\frac{h_w}{t_w}\right)_b$	$Z_b \times 10^3$ (mm^3)	$(M_{pr})_b$ (kN.m)	$\frac{\sum M_{pc}^*}{\sum M_{pb}^*}$
ID	520	150	10	8	7.1	62.5	1265	479.51	1.51
SID	520	150	10	8	7.1	62.5	1265	479.51	1.51

2.3. Loading protocol

The loading protocol in this study, shown in Fig. 11, was chosen according to the AISC 341–16 provisions for moment frames. This loading was applied in a cyclic manner by applying displacements to the beam end in the connection specimens (Figs. 3 & 4). The standard load history protocol proposed by the AISC 341–16 starts with applying several consecutive cycles at different story drift angles and continues with an appropriate rate of story drift increase until the connection's failure [10].

2.4. Experimental results

Laboratory observations of the specimens, including deformations, local and general buckling, whitewash flaking, as well as cracks and fractures based on the loading rate, are presented as follows:

2.4.1. Specimen 1 (ID)

By the end of the loading cycle with the story drift angle of 0.005 rad, the specimen was subjected to 12 complete loading cycles. Comparing the measured strains with the yield strain of the plates indicated an

Fig. 7. Detailing of the internal diaphragm plates [30].

elastic behavior, and no sign of whitewash flaking was seen. With the gradual increase of the loading up to the story drift angle of 0.0075 rad, whitewash flaking was observed in very small areas in the beam flanges near the beam-column interface. At the story drift of 0.01 rad, the whitewash flaking in the vicinity of the beam flange-to-column CJP groove welds increased, and it was also observed in some points of the welds themselves. At the story drift of 0.015 rad, the whitewash flaking in the beam flanges near the beam-column interface and the flange-to-column CJP groove welds further increased. With increasing hydraulic jack force and reaching the story drift of 0.02 rad, the whitewash flaking began to also occur in the column webs at the location of the continuity plates and continued to increase in the beam flanges. At the story drift of 0.03 rad, local buckling of the beam flanges started, and their first crack was observed near the beam flange-to-column groove welds.

At the story drift of 0.04 rad, the local buckling of the beam flanges increased, and they underwent local bending. Ultimately, the loading ended with the opening of the cracks in the beam flanges.

By the end of the test, except for minimal amounts in the column webs at the location of the continuity plates, no whitewash flaking was found at the panel zone, and none of the welds in the whole specimen cracked or ruptured.

The plates' yield strain values were obtained by dividing the yield stress (F_y) values from Table 1 by the modulus of elasticity (E). This strain was calculated to be 1446 με for the internal diaphragm and column wall plates, 1538 με for the beam web and 1524 με for the beam flanges. By comparing the measured strains with the calculated yield strains, it was observed that the column web in the panel zone and the middle region of the beam web next to the single shear tab behaved elastically. Moreover, as expected in the AISC provisions for the WUF-W connection, the beam flange yielded at a distance of about the beam height, leading to the formation of a plastic hinge. Fig. 12 shows the status of specimen 1 during different loading cycles.

2.4.2. Specimen 2 (SID)

By the end of the loading cycle with the story drift angle of 0.005 rad and after 12 complete loading cycles, the specimen was observed to exhibit elastic behavior with no whitewash flaking. After reaching the story drift of 0.0075 rad, whitewash flaking was observed in very small areas on the edges and the inner parts of the beam flanges near the beam-column interface. At the story drift angle of 0.01 rad, the whitewash flaking increased in the inner parts of the beam flanges near their connection to the beam web in the vicinity of the beam-to-column
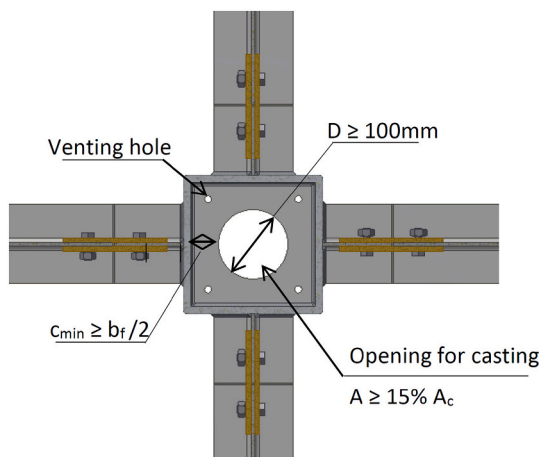
Table 5
Mixture proportions of the self-compacting concrete (SCC) used to construct the specimens (kg/m^3).

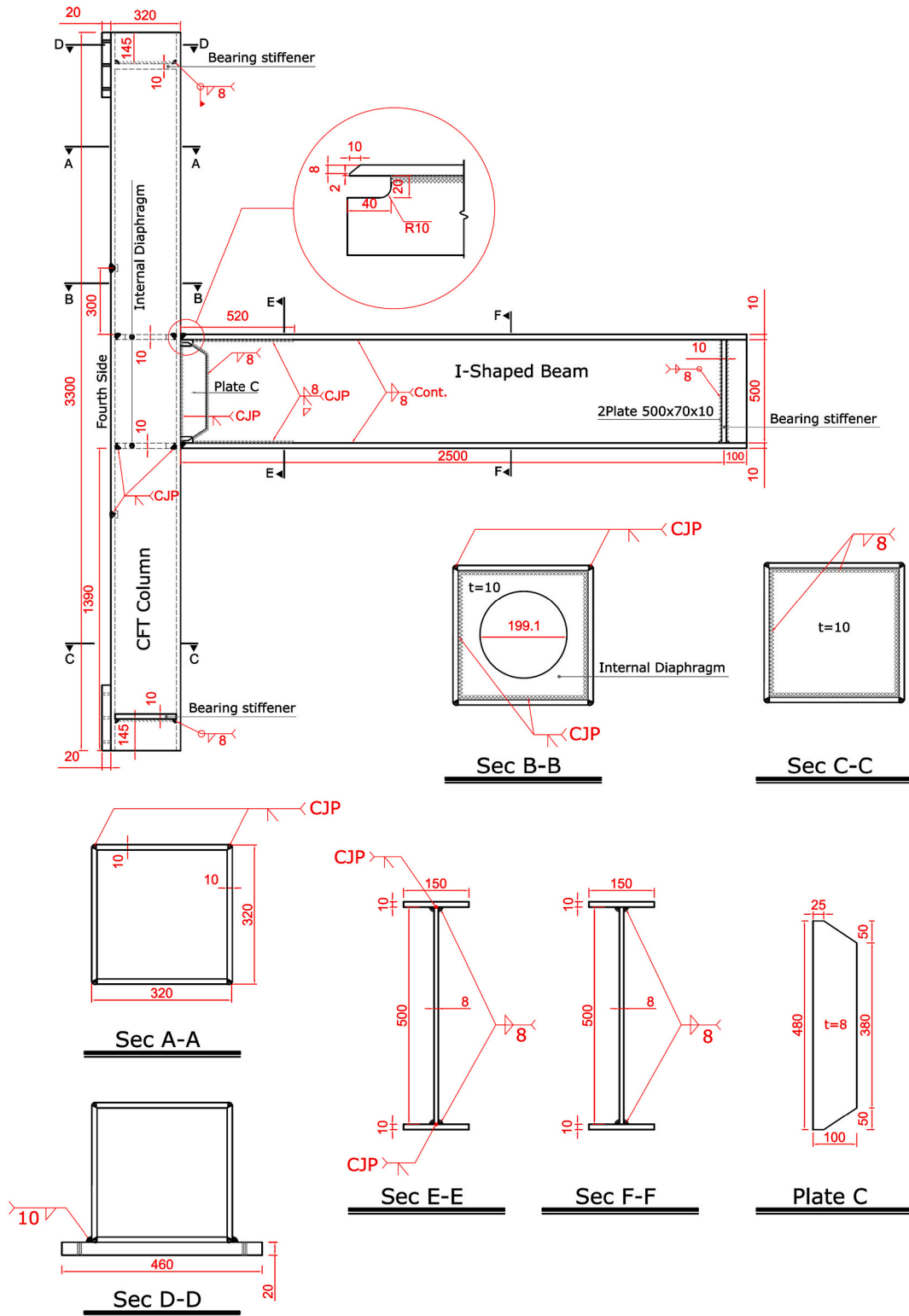| Cement	Water	Micro-Silica	Coarse aggregate	Fine aggregate	Filler Limestone powder	Superplasticizer
400	170	72	700	816	148	10

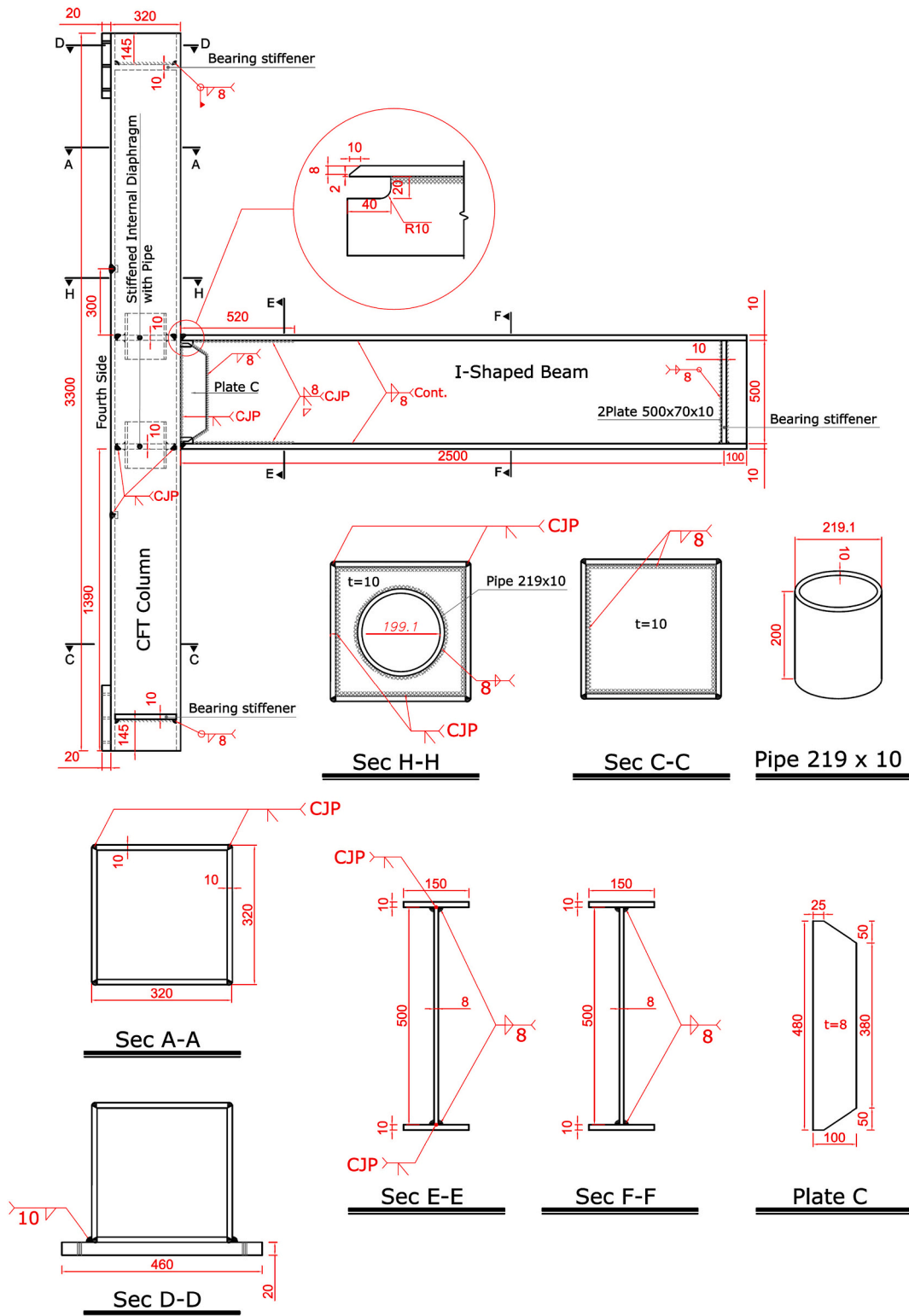**Fig. 8.** The detailed drawing of specimen 1 (ID). (Unit: mm).

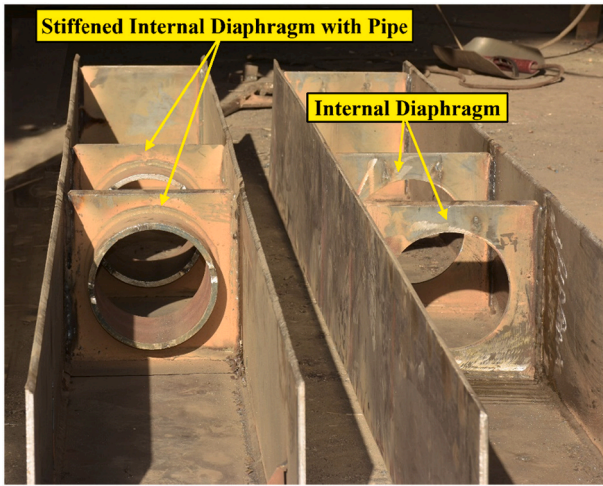**Fig. 9.** The detailed drawing of specimen 2 (SID). (Unit: mm).

Fig. 10. Columns in the specimens before the welding of plates on their fourth side.

connection. With the increase of the load applied and at the story drift angle of 0.015 rad, whitewash flaking increased near the beam flange-to-column CJP groove welds, and the beam flanges in this area became slightly distorted. At the story drift of 0.02 rad, whitewash flaking was observed in the beam flanges near the beam flange-to-column CJP groove welds and the inner parts of the beam web and flanges at a distance of about 10 cm from the beam-column interface. Also, while the distortion of the beam flanges increased, no whitewash flaking was observed in the column webs at the location of the continuity plates. At the story drift of 0.03 rad, the local buckling of the beam flanges increased, and whitewash flaking occurred in more parts of the beam flange along its length near the beam-column interface. Whitewash flaking was also observed in small areas in the CJP groove weld connecting the single shear tab to the column, and in the last cycle at this story drift, cracks started to form in the beam flanges.

At the story drift of 0.04 rad, the local buckling of the beam flanges increased further, and the experiment ended with the expansion of the cracks in the beam flanges. None of the welds in the whole specimen cracked or ruptured until the end of the test. After cutting the column at the panel zone, no cracks or damage were observed in the welds connecting the diaphragm plates to the column.

No whitewash flaking was observed in the column webs and flanges in this specimen. Also, local bending of the column flange did not occur at the connections to the beam flanges. The stiffened diaphragm plate was observed to behave appropriately, preventing the column flange from bending. Fig. 13 shows the status of specimen 2 during different loading cycles.

2.4.3. Specimens' behavior assessment

By comparing the specimens at the moment of their rupture, it was observed that the stiffening of the internal diaphragms with the pipes prevented the protruding of the column flange at its connections to the beam flanges. This indicates that in specimen 2, the stiffened diaphragms behaved well and prevented the local bending of the column flange at its connections to the beam flanges. Also, while the rupture of the beam flange in Sample 1 occurred in the vicinity of the beam flange to column CJP groove welds, this distance increased to about 5 cm in Sample 2.

Using pipes to stiffen the diaphragm plates significantly reduced their deformation and increased their stiffness. The increase in whitewash flaking along the beam flanges in Sample 2 indicates a more significant redistribution of stress at the plastic hinge in the beam, which caused the rupture location of the beam flanges to shift away from the connection.

Fig. 14 shows the hysteresis curves of the two specimens based on the beam moment at the column face and the story drift angle. The moment at the column face is the product of the force applied by the jack at the beam end and its distance from the column face. The story drift angle according to the FEMA-350 provisions is obtained by dividing the displacement applied to the beam end by the distance of the applied force to the column face plus half of the column depth [31]. The horizontal lines in the graphs indicate the moment values equal to 0.8 times the nominal plastic moment strength (M_{pb}) of the beam calculated as follows:

$$0.8M_{pb} = 0.8.Z_b.F_y = 0.8 \times 1265 \times 10^3 \times 240 = 242.88 \times 10^6 \text{ N·mm}$$

According to the hysteresis curves of the specimens, it was found that the maximum bending moment values in specimen 1 and specimen 2 were equal to 370.98 and 444.51 kN.m, respectively. Stiffening of the diaphragm plates using pipes increased the flexural capacity of the connection specimen by about 20% compared to that of the specimen without stiffening. It was observed that in both specimens, before the end of the story drift angle of 0.04 rad, the bending moment capacity of the connection was less than 0.8 times the nominal plastic moment strength of the beam. Therefore, compared to the AISC seismic
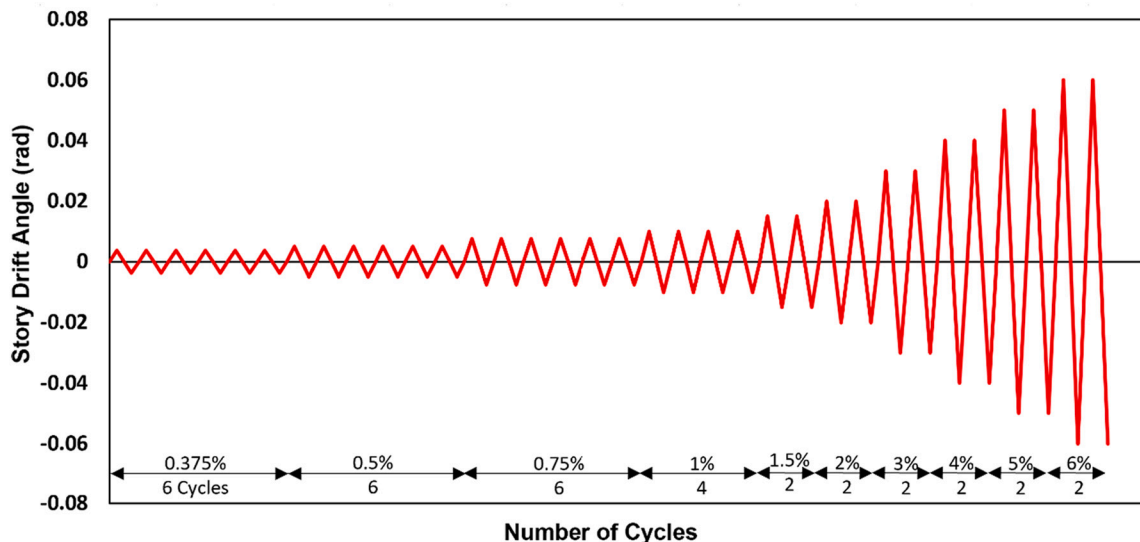

Fig. 11. Loading protocol used in the experimental testing and numerical modeling [10].

Fig. 12. Status of specimen 1 (ID) during different loading cycles.

provisions, both specimens comply with the criteria for use in intermediate and ordinary moment frames.

At the end of the test, the conditions of concrete in the panel zone and the diaphragm welds were investigated by cutting the column in the specimens. According to Fig. 15, it was found that the diaphragm welds were completely healthy, and no visible cracks or damage were observed in the concrete filling the panel zone in the specimens. Due to the local bending of the column flange at its connection to the beam flange in specimen 1 (ID), it appeared that the diaphragm in this specimen yielded in this area as shown in Fig. 15. However, no local bending of the column flange was observed in the stiffened specimen 2 (SID), indicating that utilizing the pipes effectively increased the stiffness of the diaphragms and prevented their yielding.

2.4.4. Backbone curves

In Fig. 16, the specimen's backbone curves are illustrated based on the beam moment at the column face and story drift angle. Both curves are linear and elastic and coincide up to the story drift of 0.005 rad. Therefore, the stiffening of the diaphragms with the pipes had no effect until the connection components entered the inelastic range. Nonetheless, after the story drift of 0.005 rad, it led to increasing stiffness and strength in specimen 2 compared to specimen 1.

2.4.5. Energy dissipation

Structures' resistance against earthquakes greatly depends on their energy dissipation capacity. The more energy is dissipated, the better the performance of the structure. An important indicator in evaluating the seismic performance of a connection is the determination of cumulative dissipated energy equal to the total energy dissipated up to the nominal rupture point. The cumulative dissipated energy increases with the number of load cycles. To calculate the cumulative dissipated energy, the absolute value of the area enclosed by each hysteresis loop is determined, and then these values are added together. Fig. 17 presents the curve for the cumulative dissipated energy in each loading cycle of the specimens. It can be seen that this value was equal for both samples until the 22nd loading cycle, and therefore, until the end of the story drift angle of 0.01 rad, the stiffening of the diaphragm plates with the pipes did not affect the connection's dissipated energy. Nonetheless, the cumulative dissipated energy values in the last loading cycle (story drift angle of 0.04) in specimen 1 (ID) and specimen 2 (SID) were equal to 107.8 and 131.4 kJ, respectively. Therefore, stiffening the diaphragms increased the cumulative dissipated energy of the connection by about 22%.
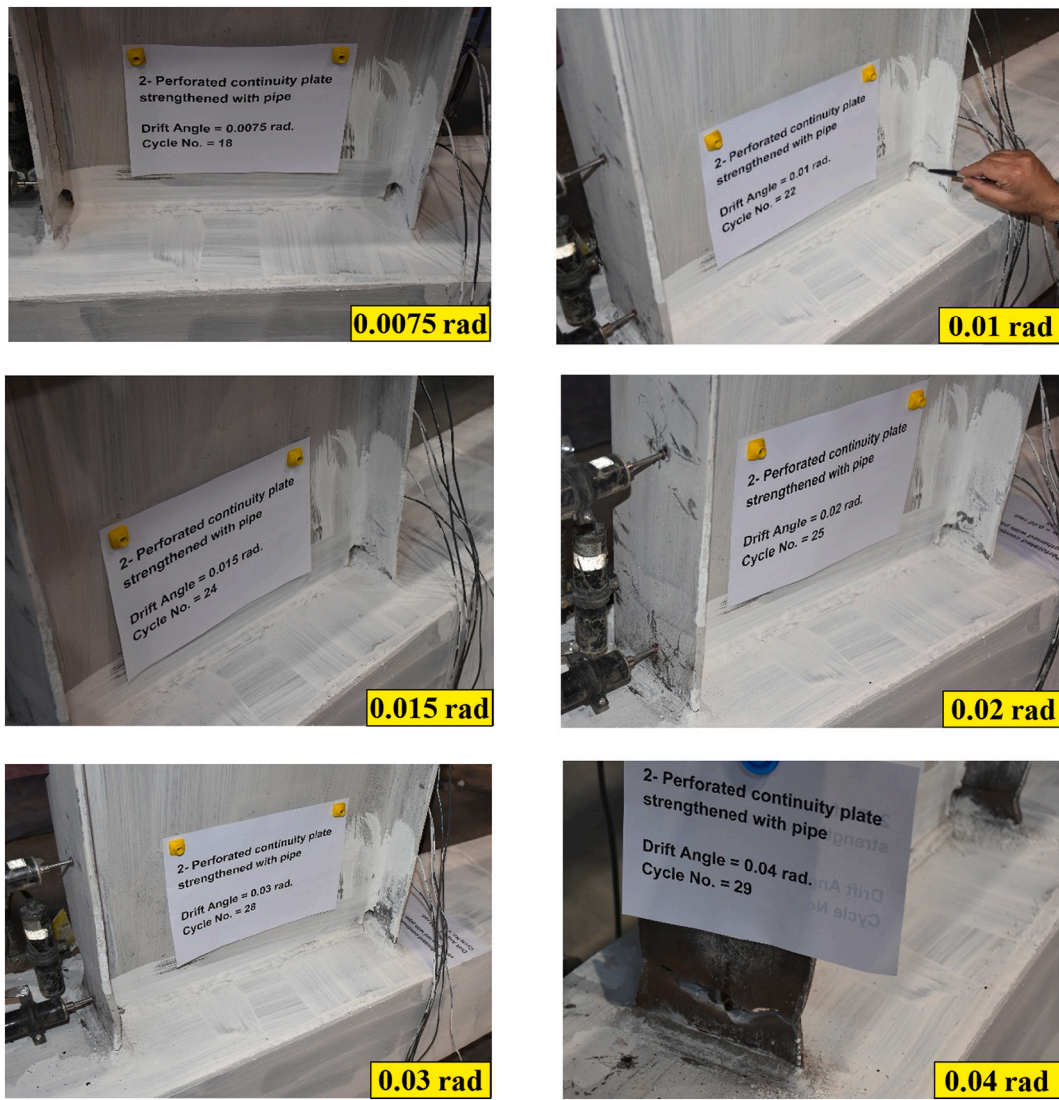
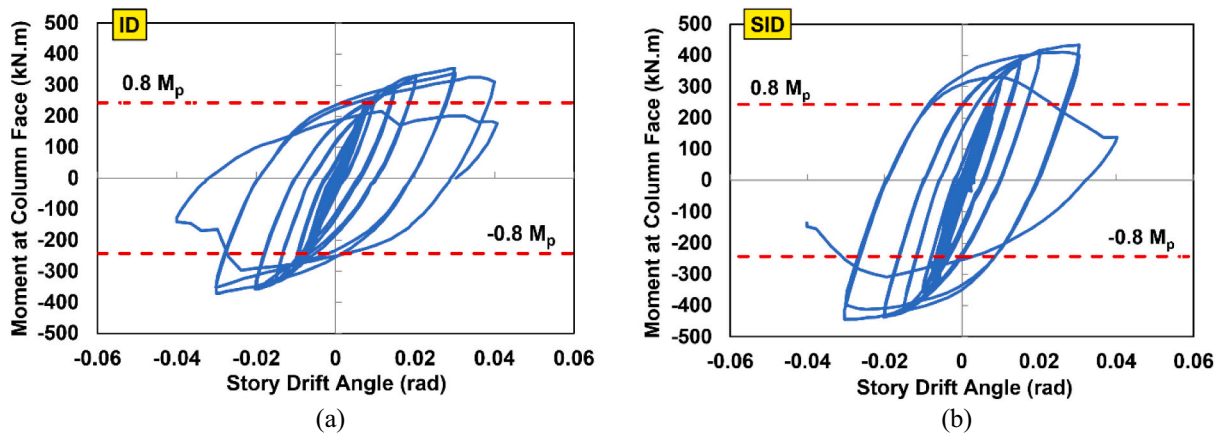**Fig. 13.** Status of specimen 2 (SID) during different loading cycles.

Fig. 14. Hysteresis curves of the tested specimens: a) Specimen 1 (ID); b) Specimen 2 (SID).

2.4.6. Stiffness degradation

Stiffness is an important parameter in the development of computational models and the study of the seismic behavior of structures. The hysteresis curves of the specimens in Fig. 14 and the backbone curves in Fig. 16 show that during the cyclic loading, the stiffness of the specimens decreases because of steel's yielding and increases failures.

Stiffness degradation is defined by the stiffness degradation coefficient (β) calculated according to the following equations [32,33]:
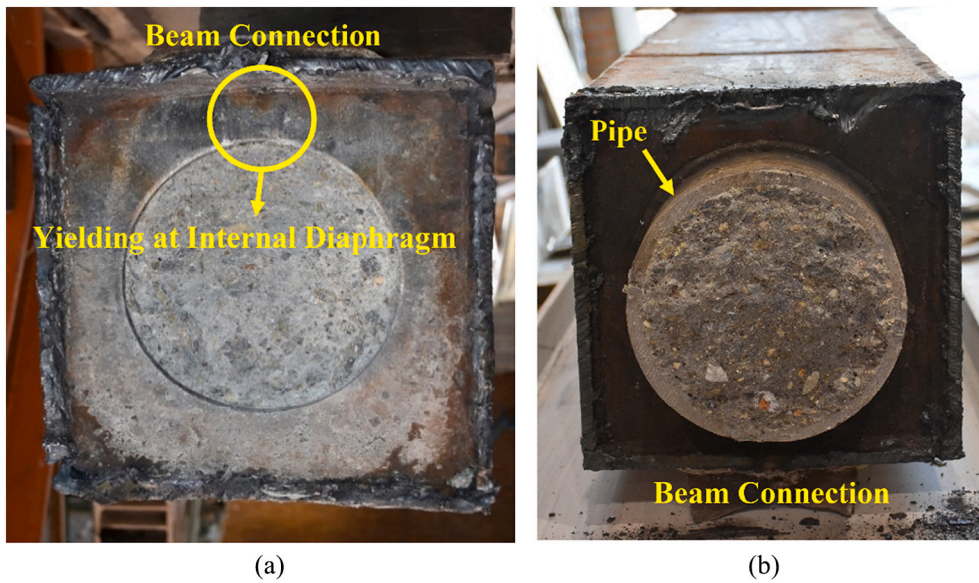
Fig. 15. Specimens cut after testing: a) Specimen 1 (ID); b) Specimen 2 (SID).

$$\beta = \frac{K_i}{K_0} \tag{1}$$

$$K_i = \frac{\sum_{j=1}^{n} M_i^j}{\sum_{j=1}^{n} \theta_i^j} \tag{2}$$

Where K_i is equal to the secant stiffness in the story drift angle i and K_0 is the initial stiffness. M_i^j is the maximum bending moment in the jth cycle of the story drift angle i and θ_i^j is the story drift angle corresponding to M_i^j. The M_i^j and θ_i^j values for the specimens were extracted from the experimental hysteresis curves.

Fig. 18 shows the stiffness degradation curves of the specimens. In relatively small story drift angles, the stiffness degradation occurred with a large slope, and by increasing the drift angle, this slope decreased. Until the story drift of 0.005 rad, the stiffness values of both specimens were approximately equal. The stiffness values decreased with the increase of the drift angle and the entry of materials into the nonlinear range. After the story drift of 0.005 rad, stiffening of the diaphragms reduced the stiffness degradation slope in specimen 2 (SID). At the story drift of 0.0075 rad, the stiffness of specimen 2 was about 8% higher than that of specimen 1. With the further increase of the story drift angle, this difference became more significant. At the story drift angle of 0.04 rad, the stiffness of specimen 2 was about 22% higher than that of specimen 1.
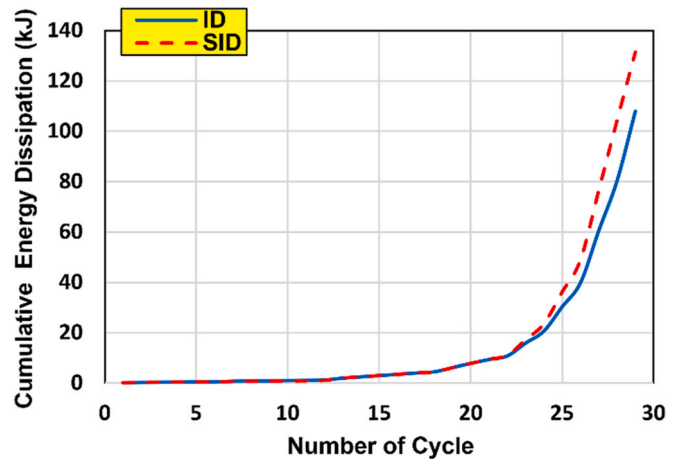

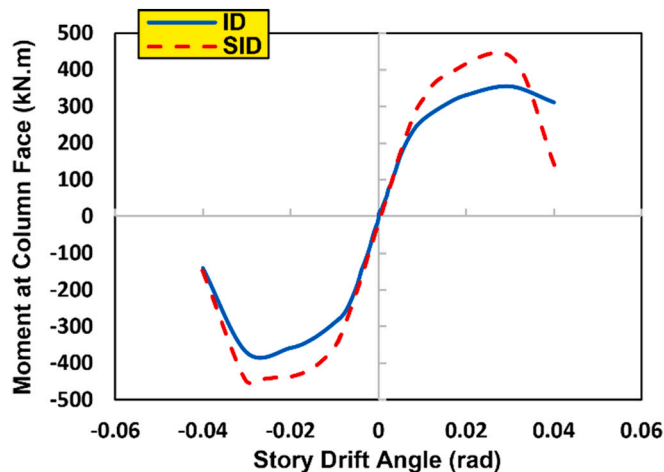Fig. 17. Cumulative dissipated energy of the specimens.
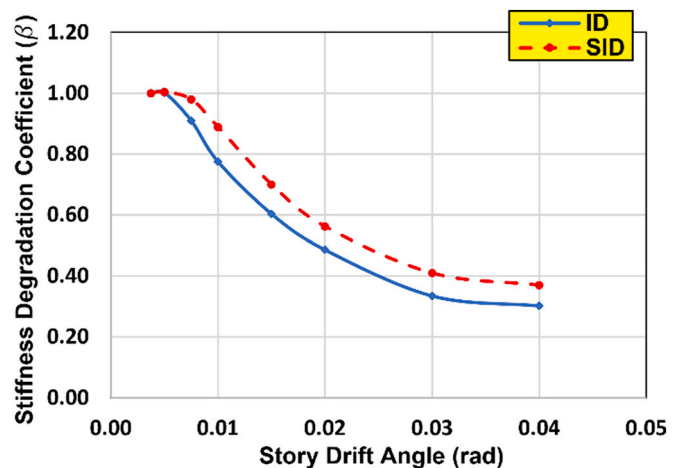

Fig. 16. Backbone curves of the specimens.

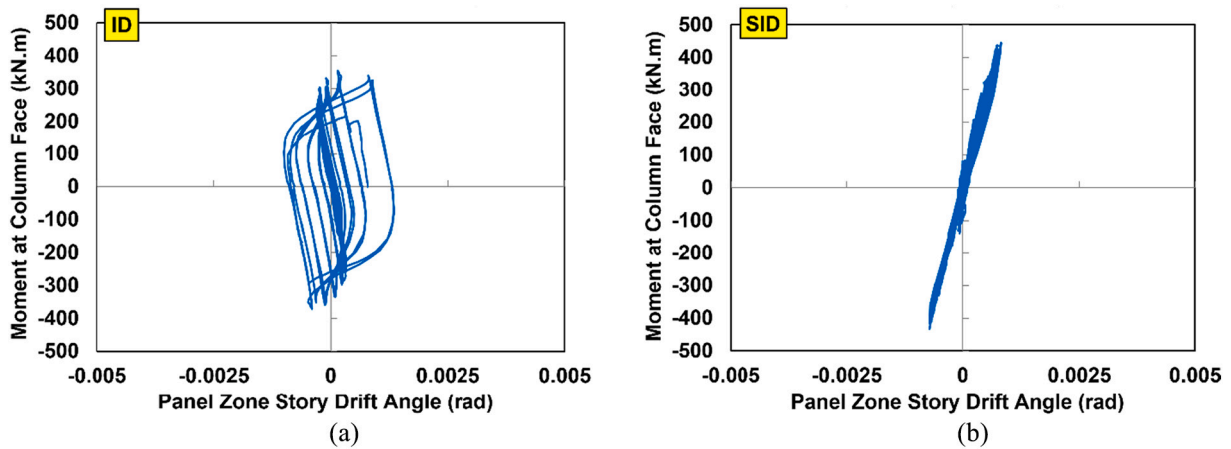Fig. 18. Stiffness degradation curves of the specimens.

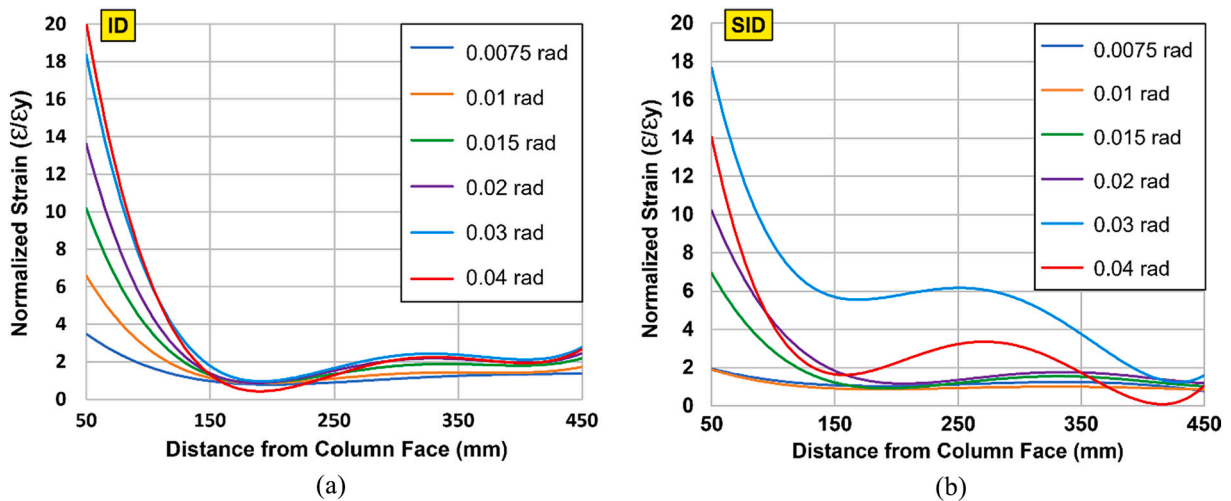**Fig. 19.** Panel zone story drift angle: a) Specimen 1 (ID); b) Specimen 2 (SID).

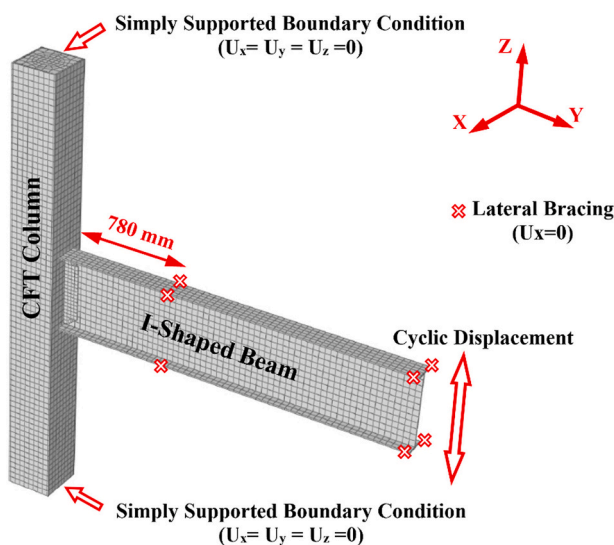**Fig. 20.** Maximum normalized strain along the length of the beam flange: a) Specimen 1 (ID); b) Specimen 2 (SID).

Fig. 21. Finite element modeling and boundary conditions.

2.4.7. Panel zone assessment

During the testing of specimen 1, a small amount of whitewash flaking occurred in the column webs at the location of the continuity plates. Nevertheless, no whitewash flaking was observed in the column in specimen 2 until the end of the loading. The deformations of the panel zones were measured by two diagonal LVDTs installed on the column webs according to Fig. 5(a). Fig. 19 shows the hysteresis curves of the specimens based on the beam moment at the column face and the panel zone story drift angle. By comparing the values of the maximum story drift in the drawn curves, it is observed that utilization of the pipes in the diaphragms of specimen 2 led to a 64% reduction in the panel zone story drift angle compared to specimen 1.

2.4.8. Beam plastic hinge assessment

Experimental results of the tested specimens showed that the in-elastic rotation of the beam at the connection region had the largest share in the overall rotation of the entire specimens.

Fig. 20 reveals the output values of the strain gauges No. 2 to 6 installed according to Fig. 5(a) at different story drift angles for the two specimens. These values were normalized with respect to the yield strain of the steel used. Until the end of the test, the maximum strain in the beam occurred in the beam flanges in the region between the beam-column interface and the end of the single shear tab of the beam web. Therefore, the presence of the single shear tab connecting the beam web to the column did not play any role in shifting the beam plastic hinge.
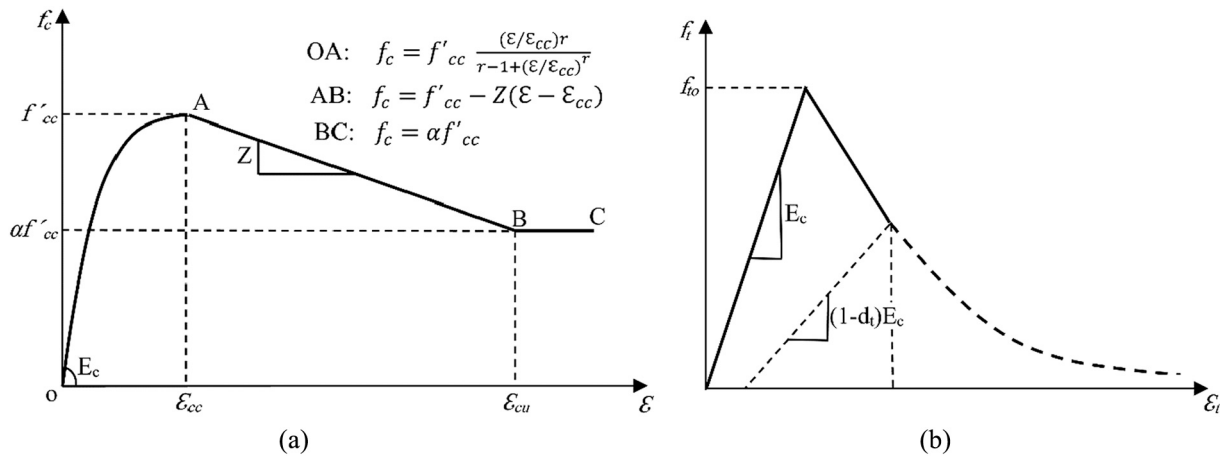
Fig. 22. Stress-strain curve of the modeled concrete: a) Compression [40]; b) Tension [48].

Considering the rupture locations of the beam flanges in the specimens, it was observed that a plastic hinge was formed near the column flange, which was predictable according to the AISC seismic provisions AISC for WUF-W connections.

As can be seen in Fig. 20, in specimen 1, after a distance of 15 cm from the column face, the strains and consequently the stresses in the beam significantly diminished, and a very high stress concentration was created near the beam-to-column connection. In specimen 2, the decrease of the strains occurred with a much smaller slope and over the whole protected zone of the beam. This indicates that the stiffening of the diaphragms resulted in better stress redistribution and reduced stress concentration in the beam flanges in the plastic hinge region.

The maximum strain values measured at the story drift angle of 0.03 rad on the beam flange and strain gauge No. 1 in specimen 1 and 2 were equal to 33,950 με (22.3 ε_y) and 95,462 με (62.6 ε_y), respectively. In the tensile test, the steel plate is subjected to uniaxial tension stress, whereas in the experimental connection, it is cyclic loading and the flange of the beam is under triaxial stress. As a result, these values are much less than the ultimate strain results shown in Table 1. Because of the multi-directional stresses have reduced the ductility of steel and its failure at a lower strain than the ultimate strain. The whitewash flaking in the specimens showed that the plastic hinge length was not equal to the beam height and was less than that predicted by the provisions. It seems that the low ratio of the clear span length to the beam height reduced the beam plastic hinge length in both specimens.

Increasing the beam height is the most critical parameter in controlling the story drift in buildings with a moment frame system as it reduces the plastic hinge length and the plastic rotational capacity of the beam.
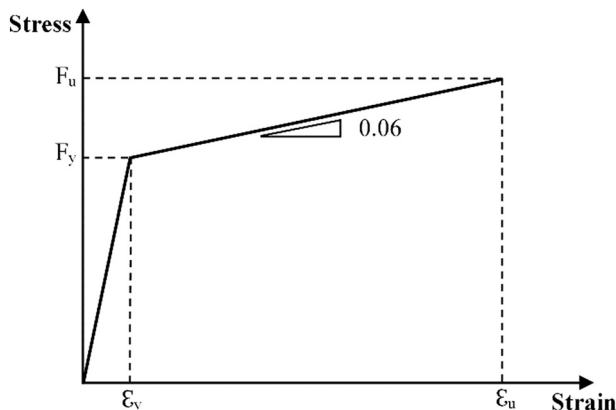

Fig. 23. Stress-strain curve of the modeled steel [41].

According to the results, in specimen 1 (ID), the strain values decreased faster at the story drift angles of 0.03 and 0.04 rad. In specimen 2 (SID), the stress in the diaphragm plates was reduced by the pipes transferring some of the diaphragm force to the concrete. Therefore, stress redistribution occurred in the beam plastic hinge rather than the continuity plates and the panel zone.

According to the installation of strain gauges on the outer surface of the beam flanges shown in Fig. 5(a), the measured strain values are only valid for those points and differ from the average strain of the plate. This difference could be considerable in case local buckling occur.

3. Numerical investigation

3.1. Modeling

In order to investigate the tested specimens numerically, they were modeled and analyzed in the Abaqus software. This software can analyze models by considering the nonlinear geometric and material effects. As shown in Fig. 4, in the experimental specimens, the column is connected to the strong floor at both ends using hinge supports, and the beam has lateral bracings at distances of 78 cm and 250 cm from the column face. According to the AISC 341–16 loading protocol, displacement was applied to the beam end using a hydraulic jack. Figs. 5(a) and 21 show the specifications and boundary conditions in the experimental specimens constructed and the FE model generated. The beam and column section dimensions, the location of the beam's lateral bracings, support conditions at the two column ends and the loading protocol applied were all modeled according to the experimental specimens and the testing conducted.

The concrete damage plasticity model was used to model the concrete inside the CFT column [34–37]. This model uses the combination of isotropic tension and plastic compression to display the nonlinear behavior of the concrete and defines stiffness degradation by considering the plastic strain in tension and compression. This model is continuous and based on plastic behavior for the concrete in the damaged state and the failure mechanisms assumed are tensile cracking and compressive crushing.

Extensive studies were carried out on confined concrete, and several papers, including those by Mander et al. [38], Liang [39] and Susantha et al. [40] presented different behavior curves for this material. In this study, the model proposed by Susantha et al. [40] was used to define the stress-strain curve of the molded concrete as shown in Fig. 22(a). This model was proposed for concrete-filled steel tube sections and verified with many experimental specimens.

Although there are different behavior models for the tensile phase of concrete, there is not much difference in the results due to the very
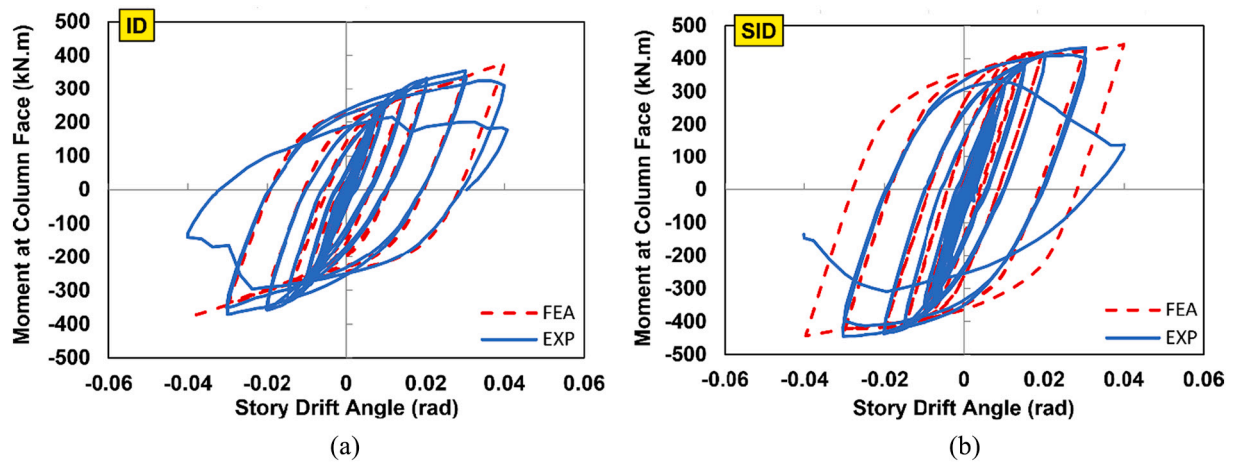
Fig. 24. FEA and experimental hysteresis curves: a) Specimen 1 (ID); b) Specimen 2 (SID).

brittle behavior of concrete in this phase. Usually, the tensile strength of concrete is considered between 7% and 10% of its compressive strength, and 10% of the compressive strength is assumed in this research. It is noticeable that unlike the compressive behavior of concrete, in the tensile state of concrete, it loses its strength suddenly with a large slope and reaches zero strength (Fig. 22(b)). However, the Abaqus software automatically considers 1% of the tensile strength of concrete in the calculations to avoid the divergence problem, even if the tensile strength is assigned zero in the software. Considering the stress-strain curve of concrete, unlike the compressive behavior, tensile behavior is elastic and linear before the maximum tensile strength [48].

In numerous studies that are similar to this one, ideal bilinear or trilinear curves have been utilized for the steel stress-strain curve in finite element analysis, which have a good agreement with experimental results and reduces the time and cost of analysis [25,34,41–44]. As shown in Fig. 23, to consider the nonlinear behavior of steel, the bilinear stress-strain relationship was used [41]. This model considers the strain-hardening effects. In the Abaqus model, for all the steel components in the elastic range, the young's modulus (E) and Poisson's ratio (ν) were considered as 200 GPa and 0.3, respectively. Stress-strain variation in the plastic region is usually considered linear with the slope between 1% and 10% of the elasticity modulus, and it was considered equal to 0.06E in this study. The yield stress and ultimate stress values of the steel plates

and pipes obtained from the standard tensile test are presented in Tables 1 and 2. These values were used to define the steel material specifications in the modeling software.

The key parameters used in the FE models, such as dilation angle (ψ), flow potential eccentricity (e), ratio of the biaxial compression strength to uniaxial compression strength of concrete (f_{b0}/f_{c0}), the ratio of the second stress invariant on the tensile meridian to that of the compressive meridian (K_c) and viscosity parameter are 31, 0.1, 1.16, 0.67, 0.001, respectively.

Solid elements, which can accurately determine the stress levels, were used in 3D modeling of the steel and concrete components. The 20-node quadratic brick with reduced integration (C3D20R) elements was employed in modeling the steel parts, which are suitable for plasticity and large deformation. For modeling the concrete core of the column, the 8-node linear brick elements with reduced integration (C3D8R) were used. Moreover, mesh sizes of 40 mm for the beam and column elements, 30 mm for the internal diaphragm and pipe elements, and 25 mm for shear tab elements (considering the mesh convergence study) were taken into account to examine the cyclic behavior of connection.

To model the behavior of the contact surfaces of the concrete core and the CFT column steel walls in the normal direction, the hard contact formulation was used. With the application of this formulation, the penetration of concrete and steel into each other and the transfer of
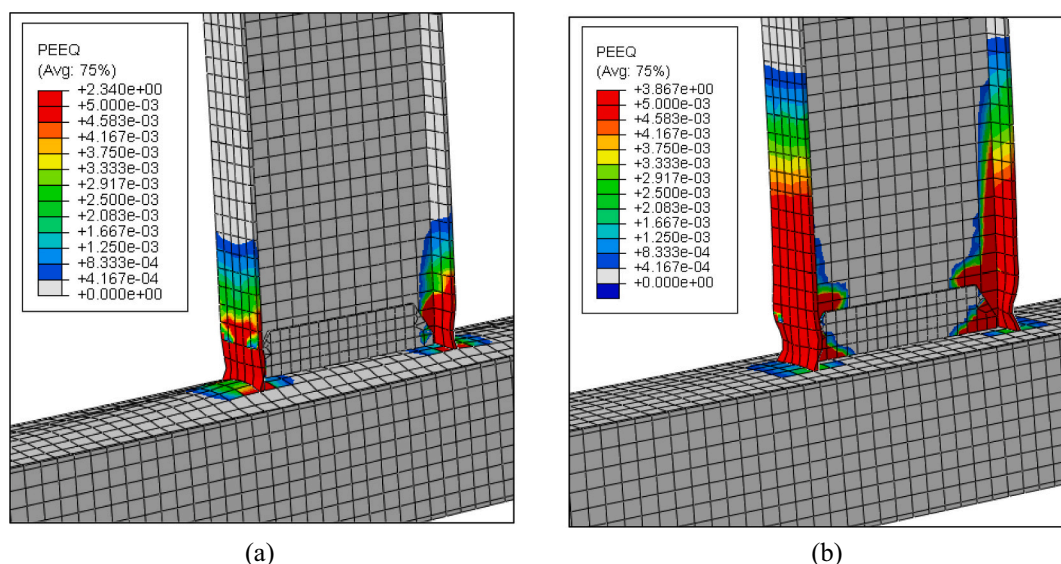

Fig. 25. Numerical analysis of the plastic equivalent strain (PEEQ) and deformations at story drift angle of 0.04 rad: a) Specimen 1 (ID); b) Specimen 2 (SID).

tensile stress along the bound sections is not possible. The materials and surface roughness affect the friction coefficients (μ). Different friction coefficients, ranging from 0.2 to 0.6, were assumed to exist in the tangential direction [45–47]. however, a sensitivity analysis revealed that while using different friction coefficients had little impact on hysteresis curves. By changing the friction coefficient from 0.2 to 0.4, the maximum bending moment values in specimen1 increases by only 1.15% and the change of this coefficient from 0.2 to 0.6 leads to an increase of about 2.49% in the bending moment capacity. For specimen 2, by changing the friction coefficient from 0.2 to 0.6, the bending moment capacity of the connection increase by 1.5%. Smaller friction was more likely to cause convergence issues in plastic deformation. For the surface between the concrete core and steel tube, a friction coefficient of 0.3 is found from the sensitivity study to enable quick convergence and get satisfactory results.

The tangential behavior formulation with the penalty option was used in the tangential direction of the concrete and steel contact surfaces, which considers the friction force created by applying the friction coefficient between the steel walls and the concrete core. The interaction between the steel and concrete in the column was considered as surface-to-surface contact, and the natural cohesion between them was neglected [48].

Considering that the welds in the specimens did not rupture, it was evident that welds could not be assumed to determine the connection capacity. Therefore, tie constraints were used to connect the surfaces welded together in the FE modeling.

In the conducted numerical analysis, the general method of static analysis and direct equation solver.

with full Newton solution technique was used. The best and most reliable model was obtained after some trial-and-error cycles and different model generations.

3.2. Numerical results of experimental specimens

The hysteresis curves of the numerical analysis and experimental testing of the specimens up to the moment of rupture are compared in Fig. 24. The FE hysteresis loops almost coincide with the experimental loops in terms of bending moment capacity and stiffness up to the story drift angle of 0.03 rad. However, at the story drift of 0.04 rad, the cracks created in the beam flanges reduced the resistance in the specimens, leading to differences in the hysteresis curves from experimental testing and numerical modeling.

The second-order element meshing suitable for large strains and deformations with stress concentration was used to model the beam flanges. In this type of meshing, the residual plastic deformations due to the compressive loads from bending moment led to out-of-plane

deformation of the beam flanges at the plastic hinge location. Fig. 25 shows the deformation of FE models at the story drift angle of 0.04 rad, and Fig. 26 indicates the failure of the specimens. It can be seen that the deformation of the beam flanges at the plastic hinge and the local bending of the column flange at the connections to the beam flanges are similar in the numerical models and experimental specimens. Therefore, the proposed numerical model could be suitably used to study the seismic behavior of I-beam to CFT column moment connections. However, due to the factors such as geometric differences, the exact application of boundary conditions in the Abaqus model, uncertainties in modeling the mechanical behavior of materials and residual stresses, there are some differences between the FEA and experimental results.

3.3. Rupture index (RI) of experimental specimens

In order to investigate the fracture potential at each point of the connection, the rupture index (RI) was calculated by substituting the FEA results into Eqs. 3 and 4 [49]. Assessment of the specimens indicated that points on line AB on the top beam flange at the connection to the column had a high stress concentration (Fig. 27). For a more detailed inspection, the rupture index was calculated in the points corresponding to the elements on this line. An increase in the rupture index of each
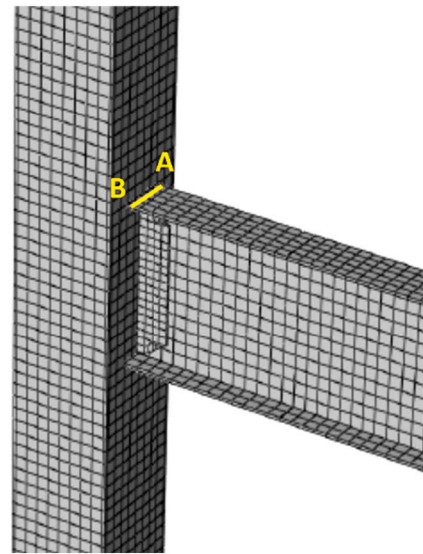
Fig. 27. Line AB marked to check the rupture index at the beam-column interface.
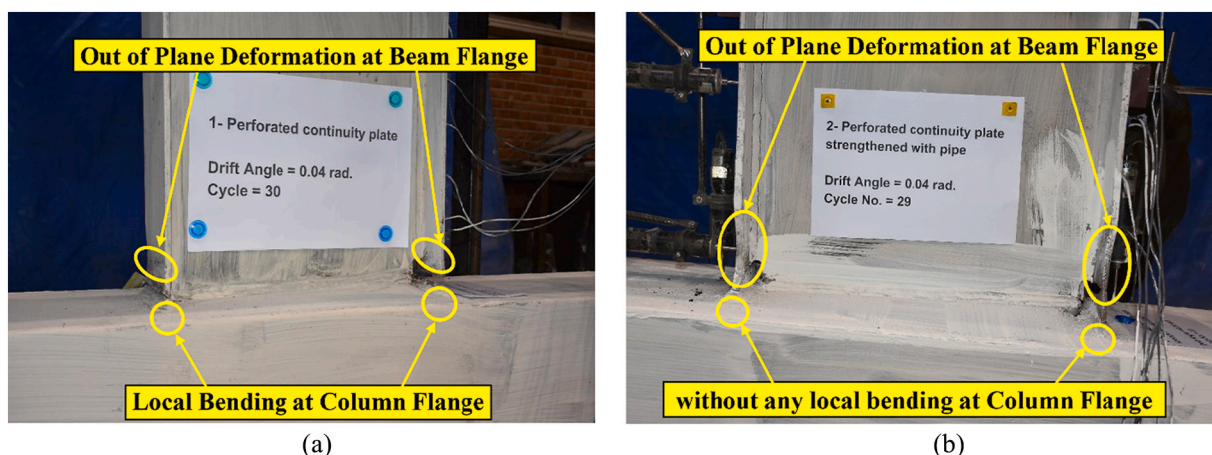
(a)   (b)

Fig. 26. Experimental results at drift angle of 0.04 rad: a) Specimen 1(ID); b) Specimen 2 (SID).

point increases the fracture potential. The points under the bottom beam flange at the connection to the column were also similar to those on line AB. In the experimental specimens, the reason for the cracks starting in the beam flanges at a short distance from the beam-to-column welds was the higher strength of the CJP groove welds compared to the steel plates.

$$RI = \frac{PEEQ}{exp\left(-1.5\frac{\sigma_m}{\sigma_{eff}}\right)} \tag{3}$$

$$PEEQ = \frac{\varepsilon_p}{\varepsilon_y} \tag{4}$$

In the above relations, ε_p is the equivalent plastic strain, ε_y is the yield strain, σ_m is the hydrostatic stress, σ_{eff} is the von Mises stress, PEEQ is the plastic equivalent strain index, and $\frac{\sigma_m}{\sigma_{eff}}$ is the triaxiality ratio (TR). Increasing the triaxiality ratio reduces the rupture strain of a given material significantly and thus limits its ductility.

Fig. 28 shows the rupture index results for the Abaqus models generated in this study. As can be observed, sample 1's largest rupture index occurred at the beam flange's outside edges, but sample 2's maximum rupture index happened close to the center of the flange's width. Fig. 29 depicts the beginning of both experimental connections' failure, which is completely consistent with the conclusions of the finite element model. It should be noted that in sample 1, the diaphragm's circular hole has caused stiffness changes in this plate and the back part of the beam flange. Given that the hole is in the center of the diaphragm, the stiffness of this part has diminished, which results in less of it being

able to withstand the force of the connection moment. As a result, the rupture index in the center of the beam flange width is decreased. In sample 2, the employment of the pipe increased the diaphragm plate's middle portion's stiffness relative to its side portions, which led to an increase in the rupture index in the middle of the beam flange's width.

3.4. Parametric analysis of models

This section examines the effects of altering various parameters on the moment capacity and the cumulative dissipated energy of the connections via FE simulations on the models validated in the previous section. For this purpose, changes in the diameter and thickness of the internal diaphragm and the effect of concrete inside the column tube have been examined in the laboratory connection of sample 1 and changes in the height and thickness of the pipe and the effect of concrete inside the CFT column have been examined in sample 2 (SID). Similar to the numerical models of laboratory connections, the remaining specifications in these models include the sizes of the beams and columns, the loading, the stress-strain curves for steel and concrete, the friction coefficient, etc. The loading protocol of the AISC 341–16 regulation is applied to the models up to cycle number 30, which corresponds to the end of the story drift angle of 0.04 rad, taking into account that the maximum story drift angle of the tested samples before rupture is equal to 0.04 rad. Fig. 30 compares the findings of the bending moment of the connection at column face and cumulative energy dissipation for sample 1 (ID) using a bar chart, and Fig. 31 presents the same results for sample
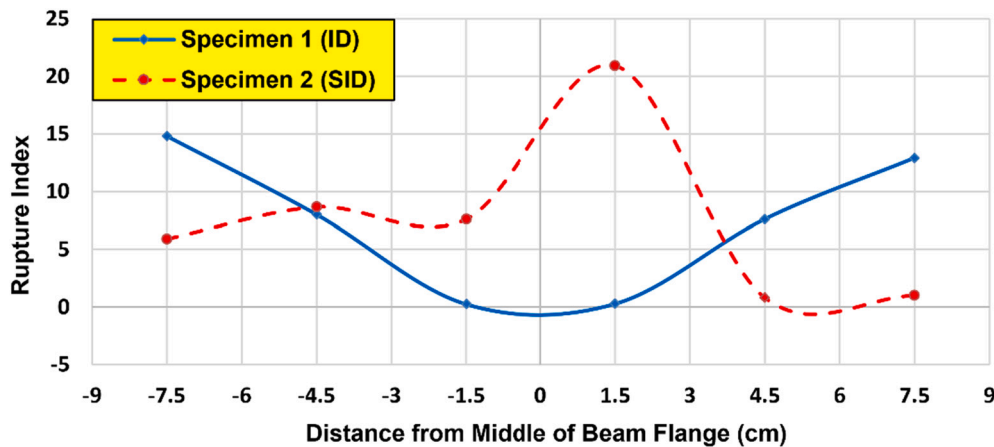

Fig. 28. Comparison of the rupture index on the AB line for specimens 1 and 2.

(a)   (b)

Fig. 29. Location of failure on the beam flange: a) Specimen 1(ID); b) Specimen 2 (SID).
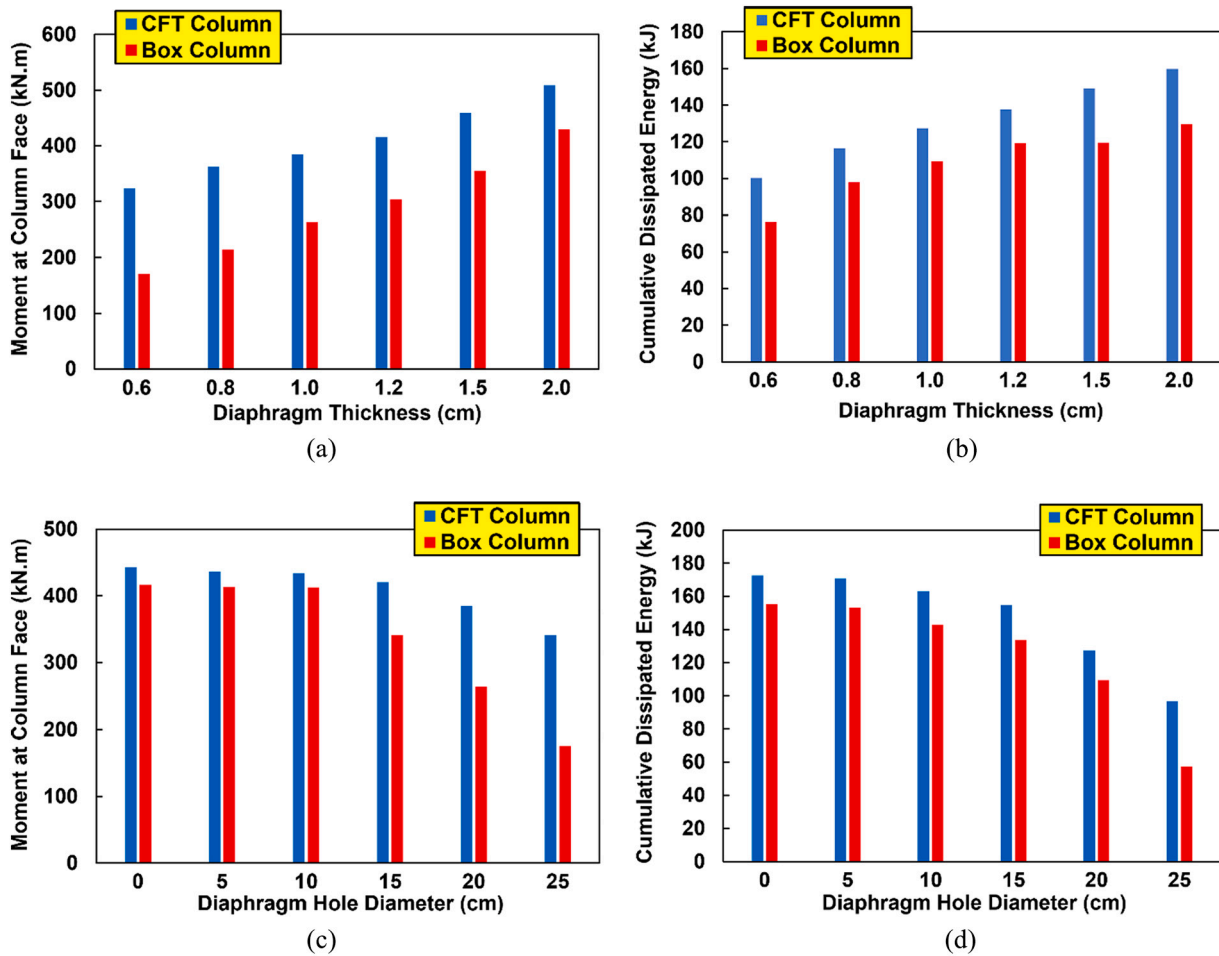
Fig. 30. Comparison of moment at column face and cumulative dissipated energy in Specimen 1(ID): a) & b) Effect of diaphragm thickness; c) & d) Effect of diaphragm hole diameter.

2 (SID) with a change in pipe specifications.

As illustrated in Fig. 30 (a & b), increasing the internal diaphragm thickness from 0.6 cm to 2 cm resulted in a 153% increase in flexural capacity when I-beam connected to the box column and a 57% increase when I-beam connected to the CFT column. Also, the use of concrete inside the box column, in the usual case of using a diaphragm with the same thickness as the beam flange, has caused an increase of about 46% in the bending moment and 16.5% in the cumulative energy dissipation of the connection. It should be noted that using an internal diaphragm with a significant thickness can result in residual stresses in the column wall and increase welding volume and expense. It is advantageous to use CFT columns rather than box columns in structures because by using concrete inside the column, the lowest increase in the flexural capacity of the connection by using an internal diaphragm with a thickness of 2 cm is equal to 18%. In other words, by increasing the thickness of internal diaphragm, the influence of concrete reduces and the positive effect of concrete for the thickest internal diaphragm in increasing the flexural capacity of connection is 18%. For thinner thickness this percent increases. Fig. 30 (c & d) shows that extending the internal diaphragm hole diameter to 25 cm while employing a CFT column instead of a box column enhances moment capacity by around 95% and cumulative dissipated energy of connection up to 69%. From a practical standpoint,

the key consideration in selecting the internal diaphragm hole's diameter is to facilitate the passage of concrete inside the column tube and fill the panel zone with concrete, which should be considered in the design of the CFT column.

As seen in Fig. 31 (a & b), increasing the height of the pipe up to 10 cm results in a significant increase in the bending moment and energy absorption of the connection. As the pipe's height is increased further, the increase in bending capacity and energy absorption continues with a very slight slope as it is anticipated. It is obvious that increasing the height of the pipe increases the stiffness and strength of the perforated continuity plate, yet this increase can improve the beam-to-column connection performance more effectively to a certain extent. Additionally, the presence of concrete inside the column has increased the bending moment and cumulative energy dissipation by at least 24%. In the sample with the CFT column, raising the pipe thickness from 0.63 cm to 2 cm only resulted in an increase of 3.8% in the connection's bending moment, as shown in Fig. 31 (c & d). Increasing the thickness of the pipe to stiffen the internal diaphragm does not appear to be a suitable approach to improve the performance of the connection. Instead, it appears that utilizing a pipe with the appropriate height can increase the stiffness and strength of the diaphragm adequately.
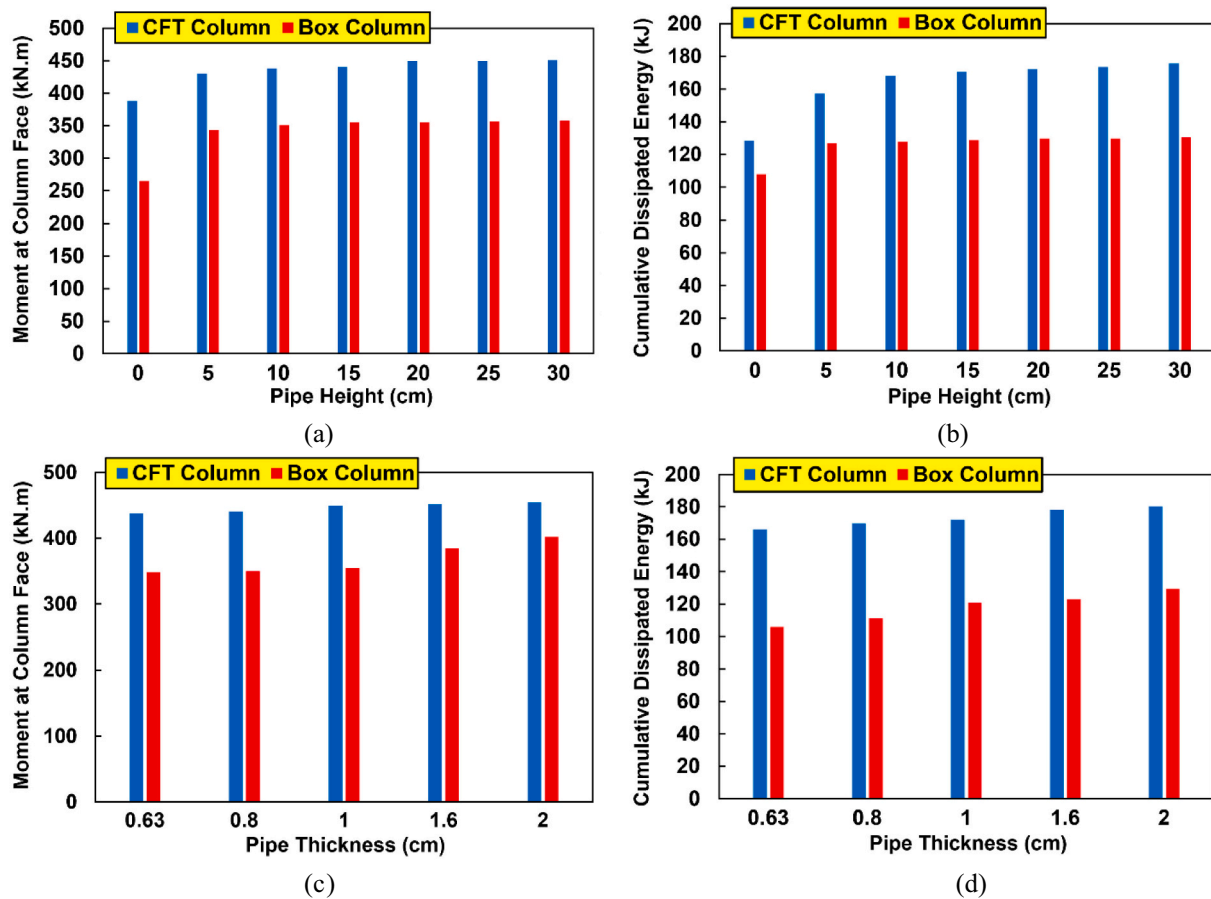
Fig. 31. Comparison of moment at column face and cumulative dissipated energy in Specimen 2(SID): a) & b) Effect of pipe height; c) & d) Effect of pipe thickness.

4. Conclusion

This study investigated the seismic behavior of the two full-scale I-beam to CFT column moment connection specimens. Then the experimental samples were analyzed by the finite element method and parametric studies were done on the specimens in the Abaqus software. The most important results of this research are as follows:

1- The hysteresis curves of the specimens showed that stiffening the internal diaphragms with the pipes caused a 20% increase in the flexural capacity of the connection and a 22% increase in the cumulative energy dissipation.

2- Utilization of stiffened diaphragms in specimen 2 prevented the yielding of these plates and reduced the stress concentration in the beam flanges at the connection to the column. It also caused a 5 cm shifting of the rupture location in the beam flanges compared to specimen 1. The occurrence of no yielding in the diaphragms did not cause the local bending of the column flange at the connection to the beam in specimen 2.

3- Using the pipes to stiffen the diaphragms in specimen 2 led to a 64% reduction in the panel zone story drift angle compared to specimen 1 and therefore increased the story drift share of the beam. Besides, by increasing the drift angle, stiffening the diaphragms increased the connection stiffness by 8% to 22%.

4- By stiffening the diaphragms with pipes, the corresponding location of the maximum rupture index (RI) was shifted away from the outer edge of the beam flange for about 40% of the beam flange width towards the longitudinal axis of the beam. This shifting resulted in better stress redistribution across the beam flange width.

5- Although stiffening of the diaphragms in specimen 2 increased the flexural capacity of the connection and led to better stress distribution in the beam flanges, considering the story drift angle capacity of the connection at the moment of rupture and comparison with the AISC seismic provisions, this connection can be suitably utilized in intermediate moment frames but cannot be utilized in special moment frame systems.

CRediT authorship contribution statement

Alireza Habibi: Investigation, Software, Writing – original draft. **Nader Fanaie:** Conceptualization, Methodology, Supervision. **Shahriar Shahbazpanahi:** Validation, Data curation, Visualization, Writing – review & editing.

Declaration of Competing Interest

The authors whose names are listed immediately below certify that they have no affiliations with or involvement in any organization or entity with any financial interest (such as employment, patent-licensing arrangements, etc.), or non-financial interest (such as personal or professional relationships, affiliations, knowledge or beliefs) in the subject matter discussed in this manuscript.

Data availability

Data will be made available on request.

References

[1] E. Inai, A. Mukai, M. Kai, H. Tokinoya, T. Fukumoto, K. Mori, Behavior of concrete-filled steel tube beam columns, J. Struct. Eng. 130 (2) (2004) 189–202, https://doi.org/10.1061/(ASCE)0733-9445(2004)130:2(189).

[2] L.-H. Han, G.-H. Yao, Z. Tao, Performance of concrete-filled thin-walled steel tubes under pure torsion, Thin-Walled Struct. 45 (1) (2007) 24–36, https://doi.org/10.1016/j.tws.2007.01.008.

[3] W.L.A. de Oliveira, S. De Nardin, A.L.H. de Cresce El, M.K. El Debs, Evaluation of passive confinement in CFT columns, J. Constr. Steel Res. 66 (4) (2010) 487–495, https://doi.org/10.1016/j.jcsr.2009.11.004.

[4] N.J. Gardner, E.R. Jacobson, Structural behavior of concrete filled steel tubes, J. Proceed. (1967) 404–413, https://doi.org/10.14359/7575.

[5] S. Morino, K. Tsuda, Design and construction of concrete-filled steel tube column system in Japan, Earthquake Eng. Eng. Seismol. 4 (1) (2003) 51–73.

[6] Y.M. Alostaz, S.P. Schneider, Analytical behavior of connections to concrete-filled steel tubes, J. Constr. Steel Res. 40 (2) (1996) 95–127, https://doi.org/10.1016/s0143-974x(96)00047-8.

[7] E. Jahanbakhti, N. Fanaie, A. Rezaeian, Experimental investigation of panel zone in rigid beam to box column connection, J. Constr. Steel Res. (2017) 180–191, https://doi.org/10.1016/j.jcsr.2017.06.025.

[8] S.M. Hosseini, R. Rahnavard, Numerical study of steel rigid collar connection affecting cyclic loading, Eng. Struct. 208 (2020), 110314, https://doi.org/10.1016/j.engstruct.2020.110314.

[9] ANSI/AISC 360-–16, Specification for Structural Steel Buildings, American Institute of Steel Construction, Chicago, 2016.

[10] ANSI/AISC 341-–16, Seismic Provisions for Structural Steel Buildings, American Institute of Steel Construction, Chicago, 2016.

[11] G. Brandonisio, A. De Luca, E. Mele, Shear strength of panel zone in beam-to-column connections, J. Constr. Steel Res. 71 (2012) 129–142, https://doi.org/10.1016/j.jcsr.2011.11.004.

[12] Y. Qin, Z. Chen, X. Wang, T. Zhou, Seismic behavior of through-diaphragm connections between CFRT columns and steel beams-experimental study, Adv. Steel Constr. 10 (3) (2014) 351–371.

[13] CECS 159, Technical Specification for Structures with Concrete-Filled Rectangular Steel Tube Members, China Association for Engineering Construction, Beijing, 2004.

[14] Z. Lai, E.C. Fischer, A.H. Varma, Database and review of beam-to-column connections for seismic design of composite special moment frames, J. Struct. Eng. 145 (5) (2019) 04019023, https://doi.org/10.1061/(asce)st.1943-541x.0002295.

[15] L. Kang, R.T. Leon, X. Lu, Shear strength analyses of internal diaphragm connections to CFT columns, Steel Compos. Struct. 18 (5) (2015) 1083–1101, https://doi.org/10.12989/scs.2015.18.5.1083.

[16] S. Yaghoobi Zadeh, N. Fanaie, Investigation on the behavior of beam to column rigid connection in concrete filled tube (CFT) in presence of perforated internal continuity plate, in: 10th Natoinal Conference On Steel & Structure, 2019. Iran.

[17] P. Doung, S. Leelataviwat, E. Sasaki, Tensile strength and failure mechanism of internal diaphragms in wide flange beam-to-box column connections with concrete filling, J. Build. Eng. 34 (2021), 102037, https://doi.org/10.1016/j.jobe.2020.102037.

[18] Y. Qin, Z. Chen, X. Wang, Experimental investigation of new internal-diaphragm connections to CFT columns under cyclic loading, J. Constr. Steel Res. 98 (2014) 35–44, https://doi.org/10.1016/j.jcsr.2014.02.014.

[19] Y.M. Xiao, T. Zhang, Parametric analysis on seismic behavior of connections to concrete-filled square steel tubular columns with three edges welded interior diaphragm, Adv. Mater. Res. Trans Tech Publ (2011) 562–566, https://doi.org/10.4028/www.scientific.net/amr.163-167.562.

[20] P. Doung, E. Sasaki, Load-deformation characteristics and performance of internal diaphragm connections to box columns, Thin-Walled Struct. 143 (2019), 106221, https://doi.org/10.1016/j.tws.2019.106221.

[21] J. Nie, K. Qin, C. Cai, Seismic behavior of connections composed of CFSSTCs and steel–concrete composite beams—experimental study, J. Constr. Steel Res. 64 (10) (2008) 1178–1191, https://doi.org/10.1016/j.jcsr.2007.12.004.

[22] J. Nie, K. Qin, C. Cai, Seismic behavior of connections composed of CFSSTCs and steel–concrete composite beams—finite element analysis, J. Constr. Steel Res. 64 (6) (2008) 680–688, https://doi.org/10.1016/j.jcsr.2007.12.003.

[23] AIJ, Recommendations for Design and Construction of Concrete Filled Steel Tubular Structures, Architectural Institute of Japan, Tokyo, 2001.

[24] O. Rezaifar, A. Younesi, Experimental study discussion of the seismic behavior on new types of internal/external stiffeners in rigid beam-to-CFST/HSS column connections, Constr. Build. Mater. 136 (2017) 574–589, https://doi.org/10.1016/j.conbuildmat.2017.01.032.

[25] B. Rong, Y. Zhang, J. Sun, R. Zhang, Experimental and numerical research on hysteretic behavior of CFST frame with diaphragm-through connections, J. Build. Eng. 45 (2022) 103529, https://doi.org/10.1016/j.jobe.2021.103529.

[26] X. Lu, L. Kang, R.T. Leon, The influence of joint details and axial force ratios on failure mechanisms of SCFT column-beam connections, J. Asian Architect. Build. Eng. 14 (1) (2015) 197–204, https://doi.org/10.3130/jaabe.14.197.

[27] S.-H. Kim, S.-M. Choi, Tensile strength and concrete cone failure in CFT connection with internal diaphragms, Int. J. Steel Struct. 17 (2) (2017) 643–652, https://doi.org/10.1007/s13296-017-6021-9.

[28] S.-M. Choi, Y.-S. Yun, J.-H. Kim, Experimental study on seismic performance of concrete filled tubular square column-to-beam connections with combined cross diaphragm, Steel Compos. Struct. 6 (4) (2006) 303–317, https://doi.org/10.12989/scs.2006.6.4.303.

[29] ANSI/AISC 358-–10, Prequalified Connections for Special and Intermediate Steel Moment Frames for Seismic Applications, American Institute of Steel Construction, Chicago, 2010.

[30] M.X. Richard Liew, Chi Trung Tran, Design Guide for Concrete Filled Tubular Members with High Strength Materials - an Extension of Eurocode 4 Method to C90/105 Concrete and S550 Steel, Research Publishing Services, Singapore, 2015.

[31] FEMA 350, Recommended Seismic Design Criteria for New Steel Moment Frame Buildings, Federal Emergency Management Agency, Washington, 2000.

[32] Y. Qin, Z. Chen, Q. Yang, K. Shang, Experimental seismic behavior of through-diaphragm connections to concrete-filled rectangular steel tubular columns, J. Constr. Steel Res. 93 (2014) 32–43, https://doi.org/10.1016/j.jcsr.2013.10.020.

[33] X. Zhang, S. Zheng, X. Zhao, Seismic performance of steel beam-to-column moment connections with different structural forms, J. Constr. Steel Res. 158 (2019) 130–142, https://doi.org/10.1016/j.jcsr.2019.03.028.

[34] R. Bhartiya, D.R. Sahoo, A. Verma, Modified damaged plasticity and variable confinement modelling of rectangular CFT columns, J. Constr. Steel Res. 176 (2021), 106426, https://doi.org/10.1016/j.jcsr.2020.106426.

[35] N. Fanaie, H.S. Moghadam, Experimental study of rigid connection of drilled beam to CFT column with external stiffeners, J. Constr. Steel Res. 153 (2019) 209–221, https://doi.org/10.1016/j.jcsr.2018.10.016.

[36] B.-Y. Li, Y.-L. Yang, Y.-F. Chen, W. Cheng, L.-B. Zhang, Behavior of connections between square CFST columns and H-section steel beams, J. Constr. Steel Res. 145 (2018) 10–27, https://doi.org/10.1016/j.jcsr.2018.02.005.

[37] Z. Tao, Z.-B. Wang, Q. Yu, Finite element modelling of concrete-filled steel stub columns under axial compression, J. Constr. Steel Res. 89 (2013) 121–131, https://doi.org/10.1016/j.jcsr.2013.07.001.

[38] J.B. Mander, M.J. Priestley, R. Park, Theoretical stress-strain model for confined concrete, J. Struct. Eng. 114 (8) (1988) 1804–1826, https://doi.org/10.1061/(ASCE)0733-9445(1988)114:8(1804).

[39] Q.Q. Liang, Performance-based analysis of concrete-filled steel tubular beam–columns, Part I: Theory and algorithms, J. Constr. Steel Res. 65 (2) (2009) 363–372, https://doi.org/10.1016/j.jcsr.2008.03.007.

[40] K. Susantha, H. Ge, T. Usami, A capacity prediction procedure for concrete-filled steel columns, J. Earthq. Eng. 5 (04) (2001) 483–520, https://doi.org/10.1080/13632460109350403.

[41] A. Rezaeian, E. Jahanbakhti, N. Fanaie, Numerical study of panel zone in a moment connection without continuity plates, J. Earthq. Eng. 26 (2) (2022) 930–948, https://doi.org/10.1080/13632469.2019.1695021.

[42] G. Li, B. Chen, Z. Yang, Y. Feng, Experimental and numerical behaviour of eccentrically loaded high strength concrete filled high strength square steel tube stub columns, Thin-Walled Struct. 127 (2018) 483–499, https://doi.org/10.1016/j.tws.2018.02.024.

[43] A.K. Dessouki, A.H. Yousef, M.M. Fawzy, Stiffener configurations of beam to concrete-filled tube column connections, Steel Comp. Struct. An Int. J. 17 (1) (2014) 83–103.

[44] B. Rong, R. Liu, R. Zhang, Z. Chen, F. Apostolos, Flexural bearing capacity of diaphragm-through joints of concrete-filled square steel tubular columns, Steel Compos. Struct. 20 (3) (2016) 487–500.

[45] L. Guo, S. Gao, C. Mu, Behaviour of MCFST column-steel beam connection with side plates in the scenario of column loss, J. Constr. Steel Res. 171 (2020), 106150, https://doi.org/10.1016/j.jcsr.2020.106150.

[46] D. Lam, X. Dai, L. Han, Q. Ren, W. Li, Behaviour of inclined, tapered and STS square CFST stub columns subjected to axial load, Thin-Walled Struct. 54 (2012) 94–105, https://doi.org/10.1016/j.tws.2012.02.010.

[47] K.A. Skalomenos, G.D. Hatzigeorgiou, D.E. Beskos, Parameter identification of three hysteretic models for the simulation of the response of CFT columns to cyclic loading, Eng. Struct. 61 (2014) 44–60, https://doi.org/10.1016/j.engstruct.2014.01.006.

[48] Abaqus Theory and User''s manuals, Dassault Syst, USA, 2017.

[49] J.M. Ricles, J. Fisher, L.-W. Lu, E. Kaufmann, Development of improved welded moment connections for earthquake-resistant design, J. Constr. Steel Res. 58 (5–8) (2002) 565–604, https://doi.org/10.1016/s0143-974x(01)00095-5.